

Glacier Algae accelerate the melting rates on the south-western Greenland Ice Sheet

Joseph M. Cook¹, Andrew J Tedstone², Christopher Williamson³, Jenine McCutcheon⁴, Andrew J. Hodson^{5,6}, Archana Dayal^{1,6}, McKenzie Skiles⁷, Stefan Hofer², Robert Bryant¹, Owen McAree⁸,
5 Andrew McGonigle¹, Jonathan Ryan¹¹, Alexandre M. Anesio¹², Tristram D.L. Irvine-Fynn¹⁰, Alun Hubbard¹³, Edward Hanna¹⁴, Mark Flanner¹⁵, Sathish Mayanna^{4,16}, Liane G. Benning^{16,17,4}, Dirk van As¹⁸, Marian Yallop³, James B. Im McQuaid⁴, Thomas Gribbin², Martyn Tranter²

¹ Department of Geography, University of Sheffield

² Center for Glaciology, University of Bristol

³ Department of Biosciences, University of Bristol

⁴ School of Earth and Environmental Sciences, University of Leeds

⁵ Department of Geology, University Centre in Svalbard

15 ⁶ Department of Environmental Sciences, Western Norway University of Applied Sciences, 6856 Sogndal, Norway

⁷ Department of Geography, University of Utah

⁸ Faculty of Science, Liverpool John Moores University

⁹ School of Geosciences, University of Sydney, Sydney, NSW 2006, Australia

20 ¹⁰ Department of Geography and Earth Science, Aberystwyth University, Wales, SY23 3DB, UK

¹¹ Institute at Brown for Environment and Society, Brown University, Providence, Rhode Island, USA

¹² Department of Environmental Science, Aarhus University, 4000 Roskilde, Denmark

¹³ Centre for Gas Hydrates and Climate, University of Tromsø, Norway

¹⁴ School of Geography and Lincoln Centre for Water and Planetary Health, University of Lincoln

25 ¹⁵ University of Michigan, Ann Arbor, Michigan, USA

¹⁶ German Research Centre for Geosciences, GFZ, Potsdam, Germany

¹⁷ Department of Earth Sciences, Free University of Berlin, Germany

¹⁸ Geological Survey of Denmark and Greenland, Copenhagen, Denmark

Abstract. Melting of the Greenland Ice Sheet (GrIS) is the largest single contributor to eustatic sea level and it is amplified by the growth of pigmented algae on the ice surface that increase solar radiation absorption. This biological albedo-reducing effect and its impact upon sea level rise has not previously been quantified. Here, we combine field spectroscopy with a novel radiative transfer model, supervised classification of UAV and satellite remote-sensing data and runoff modelling to calculate biologically-driven ice surface ablation and compare it to the albedo-reducing effects of local mineral dust. We demonstrate that algal growth led to an additional $5.5 - 8.0$ $4.4 - 6.0$ Gt of runoff from bare-ice in the south-western sector of the GrIS in summer 2016/7, representing 69 ± 13 % of the total. In localised patches with high-biomass accumulation, algae accelerated melting by up to 26.15 ± 3.77 % (SE). 2017 was a particularly high albedo year, so we also extended our analysis to the particularly low-albedo 2016 melt season. The runoff from the south-western bare-ice zone attributed to algae was much higher in 2016, at $7.3 - 10.9$ Gt, although the proportion of the total runoff contributed by algae was similar at $9 - 13$ %. Algae covered similar proportions of the exposed bare ice zone across a $10,000$ km² area around our field site in both years (57.99 % in 2016, 58.89 % in 2017), but more of the algal ice was classed as “high-biomass” in 2016 (8.35 %) than 2017 (2.54 %). This interannual comparison demonstrates a positive feedback where more widespread, higher biomass algal blooms are expected to form in high melt years where the snowline retreats further, faster, providing a larger area for bloom development and also enhancing the providence of nutrients and liquid water liberated from melting ice. Our analysis confirms the importance of this biological albedo feedback and that its omission from predictive models leads to the systematic underestimation of Greenland’s future sea level contribution, especially because both the bare-ice zones available for algal colonization and the length of the active growth season are set to expand in the future.

1 Introduction

Mass loss from the Greenland Ice Sheet (GrIS) has increased over the past two decades (Shepherd et al., 2012; Hanna et al., 2013) and is the largest single contributor to cryospheric sea level rise, adding 37 % or 0.69 mm yr⁻¹ between 2012-2016 (Bamber et al., 2018). This is due to enhanced surface melting (Ngheim et al., 2012) that exceeds calving losses at the ice-sheet’s marine-terminating margins (Enderlin et al., 2014; van den Broeke et al., 2016). Surface melting is controlled by net solar radiation, which in turn depends upon the albedo of the ice surface, making albedo a critical factor for modulating ice-sheet mass loss (Box et al., 2012; Ryan et al. 2018a). The most profound shift in albedo occurs when the winter snow retreats to expose bare glacier ice. However, there are several linked mechanisms that then modulate the albedo of the exposed ice and determine its rate of melting, including meltwater accumulation, ice surface weathering and the accumulation of light-absorbing particles (LAPs), such as soot (Flanner et al., 2007)

60 and mineral dust (Skiles et al., 2017). Photosynthetic algae and cyanobacteria also reduce the albedo of the GrIS
(Uetake et al., 2010; Yallop et al., 2012; Stibal et al., 2017; Ryan et al., 2017, 2018b). Despite being known since the late
1800's (Nordenskiöld, 1875) but their effects have not yet been quantified, mapped or incorporated into any predictive
surface mass balance models (Langen et al. 2017; Noel et al., 2017; Fettweis et al. 2017). Hence, biological growth may
play an important yet under-appreciated role in the melting of the Greenland Ice Sheet and its contributions to sea
65 level rise (Benning et al., 2014).

The snow-free surface of the GrIS has a conspicuous dark stripe along the western margin which expands and
contracts seasonally, covering 4 - 10% of the ablating bare-ice area (Shimada et al., 2016). The extent and darkness
of this "Dark Zone" may be biologically and/or geologically controlled (Wientjes et al., 2011; 2016; Tedstone et al.,
70 2017; Stibal et al., 2017). There is a growing literature demonstrating the albedo-reducing role played by a community of
algae that grow on glacier ice on the eastern (Lutz et al. 2014) and western (Uetake et al. 2010; Yallop et al. 2012; Stibal et
al. 2017; Tedstone et al. 2017; Williamson et al. 2018) GrIS. The algal community on the GrIS is dominated by
Mesotaenium berggrenii, and *Ancylonema nordenskiöldii* (Yallop et al., 2012; Stibal et al., 2017; Williamson et al.,
2018; Lutz et al. 2018; Williamson et al. 2019), which are collectively known as "glacier algae" to distinguish them from
75 snow algae and sea-ice-algae. The presence of these glacier algae reduces the albedo of the ice surface, mostly due to a
brown-purple purpurogallin-like pigment (Williamson et al., 2018; Stibal et al., 2017; Remias et al., 2012).

An equivalent albedo reduction due to algae has also been studied on snow. Worldwide, snow algal communities are
dominated by unicellular *Chlamydomonaceae*, the most abundant of which belong to the collective taxon *Chlamydomonas*
80 *nivalis* (Leya et al. 2004). These algae have been shown to be associated with low-albedo snow in Eastern Greenland (Lutz
et al. 2014) and to be responsible for 17 % of snowmelt in Alaska (Ganey et al. 2017). However, for glacier algae,
Quantification of the biological albedo reduction, radiative forcing and melt acceleration has remained elusive due to
the difficulty of separating biological from non-biological albedo-reducing processes. Further, there is a need to
determine and a lack of diagnostic biosignatures for remote-sensing, which would confirm the presence or absence of ice
85 algal growth across the melting bare ice areas of the ice sheet. For snow, remote detection has been achieved by measuring
the "uniquely biological" chlorophyll absorption feature at 680 nm (Painter et al. 2001), a broader carotenoid absorption
feature (Takeuchi et al. 2006), a normalised difference spectral index (Ganey et al. 2017) and a spectral unmixing model
(Huovinen et al. 2018). However, these signature spectra can be ambiguous for glacier algae due to the presence of the
phenolic pigment with a broad range of absorption across the UV and VIS wavelengths that obscures features associated
90 with other pigments in raw reflectance spectra, and is further complicated by the highly variable optics of the underlying ice
and mixing of algae with other impurities.

Upscaling of unmanned aerial vehicle (UAV) observations made in a small sector of the Dark Zone to satellite data was prohibited by a lack of spectral resolution and ground validation (Ryan et al., 2018). **The Dark Zone is of the order 10^5 km² in extent and is undergoing long-term expansion (Shimada et al., 2016; Tedstone et al., 2017). Quantifying the impact of algal colonization on the Dark Zone is therefore paramount.** Upscaling of unmanned aerial vehicle (UAV) observations made in a small sector of the Dark Zone to satellite data has demonstrated that “distributed impurities” including algae exert a primary control on the surface albedo, but isolating the biological effect and upscaling to the regional scale has been prohibited by a lack of spectral resolution and ground validation (Ryan et al., 2018a). Recently, Wang et al. (2018) have applied the vegetation red-edge (difference in reflectance between 673 and 709 nm) to mapping glacier algae over the south-western GrIS. However, the red-edge is potentially vulnerable to false positives due to red mineral dusts which was not discounted with ground observations in their study. Furthermore, their remote-sensing used Sentinel-3 OLCI data at a coarse ground resolution (300 m) – introducing high uncertainty due to sub-pixel surface heterogeneity - and did not account for the highly variable optics of the underlying ice, meaning there is likely large uncertainty associated with their predictions of cell abundance. Neither of these previous studies quantified the effect of glacier algae effect on albedo or melt at the regional scale.

Here, we directly address these issues, ~~resolving~~ resolving a major knowledge gap limiting our ability to forecast ice-sheet melt rates into the future. First, we use spectroscopy to quantify the effect of algae on albedo and radiative forcing in ice. We then use a new radiative transfer modelling to isolate the effects of individual light-absorbing particles on the ice surface for the first time, enabling a comparison between local mineral dust and algae and providing the first candidate albedo parameterisation that could enable glacier algae to be incorporated into mass balance models. ~~To examine~~ determine spatial coverage, we apply a supervised-classification algorithm (random-forest) to map ice algae in multispectral UAV and satellite data. Runoff modelling informed by our empirical measurements and remote-sensing observations enables us to estimate the biological contribution to GrIS runoff for the first time.

2. Field sites and Methods

2.1 Overview

In this study we present a suite of empirical, theoretical and remote-sensing data to quantify and map algal contributions to melting on the south-western GrIS. At our field site we paired spectral reflectance and albedo measurements with removal of surface ice samples for biological and mineralogical analyses in order to quantify the relationship between cell abundance

125 | and broadband and spectral albedo. Laboratory measurements of the imaginary part of the refractive index of the local
mineral dusts and the purpurogallin-type phenolic compound that dominates absorption in the local glacier algae enabled a
radiative transfer model to be developed and the albedo effects of each impurity examined in isolation and compared. At the
same time, we also undertook a sensitivity study with other bulk dust optical properties from previous literature to further
test the potential role of mineral dusts in darkening the ice surface. Furthermore, by combining albedo measurements with
130 | incoming irradiance spectra and measurements of local melt rates, we were able to estimate the radiative forcing and the
proportion of melting that could be attributed to algae in areas of high and low algal biomass (H_{bio} and L_{bio}). At our field site
we made UAV flights with a multispectral camera in order to map algal coverage at high spatial resolution. We achieved this
by reducing our hyperspectral reflectance measurements down to only those wavelengths that were also measured by the
multispectral camera and then used those data to train a random-forest (RF) algorithm to classify the ice surface into discrete
135 | categories including H_{bio} and L_{bio} . This enabled estimates of algal coverage in a 200 x 200m area at our field site. We then
retrained our classifier using the nine wavelengths detected by Sentinel-2 and used this to upscale further within the south-
western region of the GrIS using Sentinel-2 imagery. With these estimates of algal coverage from our remote-sensing
imagery and calculations of the proportion of melting attributed to algae from our field data, we were able to estimate runoff
attributed to algae using van As et al.'s (2017) runoff model. The details of each stage of our methodology are provided in
140 | the following sections 2.2 – 2.10.

2.42 Field Site

145 | Experiments were carried out at the Black and Bloom Project field site (67.04 N, 49.07 W), near the Institute for
Marine and Atmospheric research Utrecht (IMAU) Automatic Weather Station 'S6' on the south-western Greenland Ice
Sheet between 10 – 22nd July 2017. The field site location is displayed in Fig 13C. Some ancillary directional reflectance
spectra included in our remote sensing training set for the supervised classification algorithms were obtained between 15-25th
150 | July 2016 at the same field site. At the field site, we established a 200 x 200 m area for UAV mapping (centred on 49° 21'
0.50" W, 67° 4' 40.42" N) where only essential access was allowed (e.g. for placing ground control points, GCPs, for
georectifying our UAV images) and sample removal was prohibited. We also delineated an additional adjacent 20 x 200 m
area that we referred to as the "sampling strip" in which we made spectral reflectance and albedo measurements paired with
removal of samples for biological and mineralogical analyses, as detailed in the following sections. The sampling strip was
155 | subdivided into smaller subregions that were then systematically visited each day of our field season. This was necessary
because ice surface samples were destructively removed for analysis and this method ensured that each area visited had not
been disturbed by our presence on previous days. Within each sub-area we visited random points, although on many
occasions the precise location was adjusted by up to 1 m in any direction to ensure that the our spectrometer viewing area

was measuring a homogenous area of a single surface type. We also occasionally selected sites within the sampling strip to ensure each surface class was sufficiently represented in our dataset. Some ancillary directional reflectance measurements were also made at the same field site between 15 - 25th July 2016 and appended to our training dataset for supervised classification (Section 2.8).

2.23 Field Spectroscopy

At each site in our sampling strip, Albedo was measured using an ASD (Analytical Spectral Devices, Colorado) Field-Spec Pro 3 spectroradiometer with ASD cosine collector. The cosine collector was mounted horizontally on a 1.5 m crossbar levelled on a tripod with a constant height of between 30 - 50 cm above the ice surface. The cosine collector was positioned over a sample surface, connected to the spectroradiometer using an ASD fibre optic, then the spectroradiometer was controlled remotely from a laptop, meaning the operators could move away from the instrument to avoid shading it. Two upwards and two downwards looking measurements were made in a total time period of < 5 minutes at each site in close succession (~ 2 minutes) to account for any change in atmospheric conditions, although the measurements presented were all made during constant conditions of clear skies at solar noon ± 1 hour. Each retrieval was the average of > 20 site replicates. The albedo spectra are provided in full along with all environmental and instrument metadata, and the codes used to process the raw data in our data repository.

Immediately after making the albedo measurements, the cosine collector was replaced with an 8-10 degree collimating lens, enabling a nadir-view hemispheric conical reflectance factor (HCRF) measurement and an albedo measurement to be obtained for each sample surface. The instrument setup and sample surface were identical between each pair of albedo and directional reflectance measurements except that the cosine collector was swapped for the collimating lens for the viewing footprint. For HCRF measurements the upwards looking measurements were replaced with HCRF measurements of a flat Spectralon panel with the spectroradiometer in reflectance mode. This protocol was followed for every sample surface with both albedo and directional reflectance measurements taking less than 5 minutes. The directional reflectance measurements were used for the surface classifications in this paper because they better approximate the measurements made by orbital remote sensing platforms. Albedo measurements were used to estimate radiative forcing because the hemispheric measurement is most appropriate for studying energy balance as it is less affected by scattering anisotropy. We closely followed the methodology described by Cook et al., (2017b). The reason both measurement types were made is that albedo is the most appropriate measurement for determining the surface energy balance, while the HCRF is closer to the measurements made by aerial remote sensing and less sensitive to stray light reflecting from surfaces other than the homogenous patch directly beneath the sensor. We therefore used the albedo for energy balance calculations and the HCRF for remote sensing applications in this study. All post-processing and analysis of albedo and HCRF measurements were made using bespoke Python scripts that are available in our repository.

2.34 Biological Measurements

Immediately following the albedo and HCRF measurements, ice from within the viewing area of the spectrometer was removed. The sample surfaces were destructively sampled using a sterile blade and scooped into sterile whirlpak bags, melted in the dark and immediately fixed with 3% glutaraldehyde. The samples were then returned to the University of Bristol and University of Sheffield where microscopic analyses were undertaken. Samples were vortexed thoroughly before 20 µL was pipetted into a Fuchs-Rosenthal haemocytometer. The haemocytometer was divided into 4_x_4 image areas. These were used to count a minimum of 300 cells to ensure adequate representation of species diversity (where possible – low abundance samples had as few as one cell per haemocytometer). The volume of each image area was used to calculate cells per mL. Biovolume was determined by measuring the long and short axes of at least ten cells from each species in each sample using the "measure" tool in the GNU Image Manipulation Program (GIMP). The morphology of the cells in the images was used to separate them into two species: *Mesotaenium bergrenii* and *Ancylonema nordenskioldii*. These dimensions were then used to calculate the mean volume of each species in each sample, assuming the cells to be circular cylinders (after Hildebrand, 1999 and Williamson et al., 2018). The average volume was multiplied by the number of cells for each species and then summed to provide the total biovolume for each sample.

2.4 Mineral dust sample preparation

High-algal-biomass-ice samples were collected in sterile sample bags and melted at ambient temperatures (5-10°C). The thawed samples were filtered onto glass-fiber filters (0.7 µm pore size), from which the solids were removed into a glass jar using a stainless steel spatula. In 50 mL centrifuge tubes, the samples were treated using 30% H₂O₂ (w/w) (Honeywell Fluka™) to remove the organic fraction. The samples (1-2 g) were sonicated (VWR ultrasonic cleaner) in 45 mL of the H₂O₂ treatment for 10 min to disaggregate the material. The samples were left in the H₂O₂ treatment for 48 h, after which they were centrifuged for 10 min at 4000 rpm (Eppendorf centrifuge 5810). The supernatant was removed, and the H₂O₂ solution was replaced. This process was repeated up to ten times until no more organic oxidation was observed. The remaining mineral fraction was washed three times in water (Sartorius arium pro ultrapure water), with centrifugation after each wash.

A 5-mg of H₂O₂-treated sample was suspended in 10 mL of ultrapure water. The sample was sonicated to disaggregate the grains. The suspension was dispersed onto a 0.2 µm polycarbonate filter (Sartorius Track-Etch Membrane, 0.2 µm). Once dry, a section of each filter was adhered to a stainless steel SEM stub using an adhesive carbon tab. The sample was coated with 8 nm of Ir (Agar high resolution sputter coater). Samples were imaged using a Zeiss Ultra Plus field emission scanning electron microscope (FE-SEM) operated at 20kV. The PSD in each sample was determined by counting all particles in an

area of $\sim 1\text{mm}^2$ that consisted of images of 100×100 and $250 \times 250 \mu\text{m}^2$ areas that were stitched together using SmartStitch software. The particles on the individual and stitched images were counted using ImageJ2 (Rueden et al. 2017). Statistical estimations of the PSD were obtained using OriginPro 8 using a single peak fitting and a Gaussian function on the obtained histograms.

2.55 Optical properties of mineral dust and algal optical properties and radiative transfer modelling

The mineral dust sample was arranged into an optically thick layer on a microscope slide which was then pressed tightly against one aperture of a Thorlabs IS200-4 2" integrating sphere. The other apertures were covered with SM05CP2C caps and the sample reflectance was measured using the same ASD Field Spec Pro 3 as was used for field measurements. The PSD and reflectance of the sample were then used to determine the complex refractive index of the bulk mineral dust mixture by inverting the Discrete Ordinates radiative transfer model (DISORT) following the methodology of Skiles et al. (2017). Briefly, the measured reflectance is used as a target for repeated runs of the DISORT model with varying refractive indices. The refractive index that gives the lowest root mean square error across the solar spectrum is determined to be the real refractive index of the bulk mixture. This is then used to forward model the optical properties of the mineral dust using Mie scattering theory. This was undertaken for mineral dust of radii $0.01 - 10 \mu\text{m}$ at a resolution of $0.01 \mu\text{m}$. The measured PSD was then used to apply a weighted average to the estimated single scattering properties to provide a bulk refractive index for the measured mineral sample. This was then added to the lookup library for the radiative transfer model. A new radiative transfer package, BioSNICAR_GO, was developed for this study and was used to predict the albedo of snow and ice surfaces with our field-measured mineral dust, algae and mineral dusts. This new radiative transfer package was produced by making a series of major updates and adaptations to the BioSNICAR model presented by Cook et al. (2017b). The package is divided into a bio-optical scheme wherein the optical properties of light-absorbing impurities and ice crystals can be calculated using Mie scattering (for small spherical particles such as black carbon or snow) or geometrical optics (for large and/or aspherical particles such as glacier algae, larger mineral dust particles and large ice crystals) and a two-stream radiative transfer model based on SNICAR (Flanner et al. 2007) which incorporates the equations of Toon et al. (1989). This is described further in the following paragraphs and in the model documentation, and a schematic of the model structure is provided in Supp. Info 1.

To incorporate glacier algae into BioSNICAR_GO, Geometrical optics was employed to determine the single scattering optical properties of the ice algae, since they are large ($10^3 \mu\text{m}^3$: far outside the domain of Mie scattering) and best approximated as circular cylinders (Hildebrand, 1999; Lee and Pilon, 2003). Our approach is adapted from the geometric optics parameterisation of van Diedenhoven (2014). The inputs to the geometric optics calculations are the cell dimensions and the complex refractive index. The imaginary part of the refractive index was calculated using a mixing model based upon Cook et al., (2017b) where the absolute mass of each pigment in the algal cells was measured

in field samples and input into the model in mg. The absorption spectra for the algal pigments is provided in Fig 2A. We updated Cook et al.'s (2017b) mixing model to apply a volume-weighted average of the imaginary part of the refractive index of water and the algal pigments so that the simulated cell looks like water at wavelengths where pigments are non-absorbing. We consider this to be more physically realistic than having cells that are completely non-absorbing at wavelengths $> 0.75 \mu\text{m}$, especially since a water fraction (X_w) is used in the calculations to represent the non-pigmented cellular components of the total cell volume. This approach also prevents the refractive index from becoming infinite when the water fraction is zero, removing the constraint that $0 < X_w < 1$ from the bio-optical scheme in the original BioSNICAR model. Based upon experimental evidence in Dauchet et al (2015) for the model species *C. reinhardtii*, the real part of the refractive index has been altered/updated from 1.5 (in Cook et al. 2017b) to 1.4. The absorption coefficients from which the imaginary refractive index is calculated are from Dauchet et al (2015) apart from the novel purpurogallin-type phenol whose optical properties were determined empirically (Fig 2A). The calculated optical properties were added to the lookup library for BioSNICAR GO for a range of cell dimensions. For the simulations presented in this study, we included two classes of glacier algae representing *Mesotenium Bergrenii* and *Ancylonema nordenskioldii* with length and diameter and also the relative abundance of each species matching the means measured in our microscopy described in Section 2.4. In simulations not shown here we found that ice albedo was relatively insensitive to the dimensions of the cells within a realistic range of lengths and diameters. For example, in a simulation with constant ice optics (snow of constant grain size $400 \mu\text{m}$, density 400 kg m^{-3} and snowpack thickness 50 mm) and a biomass mixing ratio of 10^5 ppb in the upper 1 mm layer, changing the length of the algal cells from 10 to $40 \mu\text{m}$ changed the albedo by less than 0.004 . The albedo was more sensitive to cell diameter; with the same ice optics and biomass mixing ratio as described above and an algal cell $40 \mu\text{m}$ long, changing the cell diameter from $4 \mu\text{m}$ to $12 \mu\text{m}$ changed the surface albedo by 0.008 . This low sensitivity to cell length and diameter is likely because all of the cells considered here are large from a radiative transfer perspective. For mineral dusts, we measured the optical properties of local mineral dusts by first removing the organic matter from the impurities present in melted H_{bio} ice and measuring the particle size distribution (PSD) using scanning electron microscopy (see Supp Info 2 for full sample preparation and PSD measurement details). We then arranged the mineral dust samples into an optically thick layer on a microscope slide and pressed them tightly against the open aperture of a Thorlabs IS200-4 2" integrating sphere. The other apertures were covered with SM05CP2C caps and the sample reflectance was measured using the same ASD Field Spec Pro 3 as was used for field measurements. The PSD and reflectance of the sample were then used to determine the complex refractive index of the bulk mineral dust mixture by inverting the Discrete Ordinates radiative transfer model (DISORT) following the methodology of Skiles et al. (2017). Briefly, the measured reflectance is used as a target for repeated runs of the DISORT model with varying refractive indices. The refractive index that gives the lowest root mean square error across the solar spectrum is determined to be the real refractive index of the bulk mixture. This is then used to forward model the optical properties of the mineral dust using Mie scattering theory. This was undertaken for mineral dust of radii $0.01 - 10 \mu\text{m}$ at a resolution of $0.01 \mu\text{m}$. The measured PSD was then used to apply a weighted average to the estimated single scattering properties to provide a bulk refractive index for

the measured mineral sample. This was then added to the lookup library for the radiative transfer model. The new radiative transfer package BioSNICAR_GO was used to predict the albedo of snow and ice surfaces with our field-measured mineral dust. Since we only had two samples from southwestern Greenland, we also incorporated into our radiative transfer model published optical properties for bulk minerals by Polashenski et al. (2015). They reasoned that iron-rich hematite was the primary light-absorbing mineral in Greenland dust samples, and they simulated three hematite scenarios using low (2.7 %), median (5.6 %) and high (9.3 %) estimates for the proportion of hematite in bulk mineral samples from a literature search on Greenland Ice Sheet surface mineralogy. We refer to these samples as P1, P2 and P3 for low, median and high hematite respectively. The non-hematite component of the sample was a mixture of illite, montmorillonite, calcite, kaolinite, anthropogenic particulates and quartz. Each mineral sample had a lognormal particle size distribution ranging from 0.1 μm to 90 μm . In addition, four “global average” dusts from Flanner et al. (2007), which have typical Saharan optical properties, were also used, providing a wide range of realistic dust samples with a range from low to high red-mineral content – critical because these red minerals are most likely to a) have non-negligible albedo-reducing effects, and b) have similarly shaped spectral albedo to glacier algae. We refer to these Flanner et al. (2007) dusts as F1, F2, F3 and F4. We point out that most of the samples used to generate these bulk optical properties obtained from past literature were from snow, and there may be additional inputs to the bare-ice zone due to ablative release from Holocene age ice. Our mineralogical analyses corroborate past literature that indicate that the local bare-ice mineralogy is hematite-poor and unlikely to be of Saharan origin (Tedesco et al. 2013; Wientjes et al. 2011), and we include these dusts firstly as red end-members in our sensitivity study, and also to account for possible occasional inputs from Saharan dusts from the atmosphere.

2.6 Radiative transfer modelling

The ice optical properties in BioSNICAR_GO were also calculated using a parameterisation of geometric optics adapted from van Dienenhoven et al. (2014) instead of the Mie scattering approach taken by the original SNICAR model. A geometrical optics approach to generating ice optical properties was chosen because it enables arbitrarily large ice grains with a hexagonal columnar shape to be simulated, in order to better estimate the albedo of glacier ice where grains are large and aspherical. While the real ice surface is composed of irregularly shaped and sized grains, this approach enabled us to simulate our field spectra much more accurately and circumvented the requirements that individual grains are small and spherical that underpin Mie scattering codes. The optical properties of the ice grains are modelled using refractive indices from Warren and Brandt (2008). The radiative transfer model is a two-stream model described in full in Cook et al. (2017b) and Flanner et al. (2007). BioSNICAR_GO is a major update to the the BioSNICAR model (Cook et al., 2017b; Flanner et al., 2007) that allows the user to select to predict single scattering optical properties for ice grains, mineral dusts and algal cells whose sizes exceed the upper limit of the Mie scattering domain using geometrical optics. For the entire workflow, documentation and annotated scripts are provided in our data repository. For the radiative transfer

modelling presented in this study, the following model parameters were used: -Diffuse illumination, ice crystal side-length and length/diameter per vertical layer = 3, 4, 5, 8, 10 mm, layer thicknesses = 0.001, 0.01, 0.01, 0.01, 0.01 m, underlying surface albedo = 0.15, layer densities = 300, 400, 500, 600, 700 kg m⁻³. 300 ppm of glacier algae and mineral dust were added separately to the upper 1 mm layer to quantify their effects on the surface albedo.

2.76 Quantifying Radiative forcing and biological melt acceleration

Incoming irradiance was measured at our field site using an ASD Field Spec Pro 3 spectroradiometer; however, these data were not available at sufficient temporal resolution for our hourly IRF calculations. Therefore, we simulated incoming irradiance at hourly temporal resolution and 1 nm spectral resolution using the PVSystems solar irradiance program (<https://www2.pvlighthouse.com.au>) following Dial et al., (2018). The spectral irradiance used to calculate IRF is available in our data repository.

The biological radiative forcing was calculated by first differencing the mean albedo for algal surfaces and the mean albedo for clean ice surfaces measured at our field site. This gives the difference in albedo between the clean and algal ice surfaces, α_{diff} . The product of the difference α_{diff} and the incoming irradiance, I^{spectra} , provided the instantaneous power density (PD_{alg}) absorbed by the algae. We assume that photosynthetic processes utilise 5% of this absorbed energy – at the upper end of a realistic range for photosynthetic microalgae (Blankenship et al. 2011; Masojidek et al. 2013). The remainder of PD_{alg} is conducted into the surrounding ice, giving the instantaneous radiative forcing due to algae (IRF_{alg}). Since these cells are coloured by the purple purpurogallin pigment, we assume the reflective radiative forcing to be negligible, as demonstrated by Dial et al. (2018). IRF_{alg} was calculated at hourly intervals using incoming irradiance simulated for our field site using the PVSystems solar irradiance program (<https://pvlighthouse.com.au>) at 1 nm spectral resolution, following Dial et al. (2018). The radiative forcing was assumed to be constant between each one hour timestep, meaning the radiative forcing over one hour (HRE_{alg}) could be calculated by multiplying IRF_{alg} by 3600 s h⁻¹, assuming that instantaneous radiative forcing is equal to radiative forcing per second. Daily radiative forcing due to algae (RF_{alg}) was then calculated as the sum of HRE_{alg} between 0000 and 2300.

To calculate the algal contribution to melting (M_{alg}), IRF_{alg} was multiplied by 10⁴ to convert the radiative forcing from units of W m⁻² to W cm⁻² and then divided by the latent heat of fusion for melting ice (334 J g⁻¹) and integrated over the entire day as described above. This provided a value for the amount of melting caused by the presence of algae per day assuming the cold content of the ice to be depleted. We calculated our uncertainty by running these calculations for every possible combination of our measured algal and clean ice spectra and calculating the mean, standard error and standard deviation of the pooled results.

We corroborated these estimates using a point surface energy balance model (Brock and Arnold et al. 2000). This model predicts melting in mm water equivalent given local meteorological data and information about the ice surface albedo and roughness. We ran this model with the albedo set equal to the broadband albedo for each CI, H_{bio} and L_{bio} spectrum in our field measurements. The hourly meteorological data for 21st July 2017 used to force the model was from a Delta-T GP1 automatic weather station (<https://www.delta-t.co.uk/product/ws-gp1/>) positioned at our field site, with some additional data from the nearby IMAU S6 AWS. The difference in predicted melt between the algal surfaces and the clean ice surfaces provided the melt attributed to the presence of algae. As for the radiative forcing calculations, the uncertainty was calculated by running the energy balance model for every possible combination of algal and clean ice spectra and calculating the mean, standard error and standard deviation of the pooled results.

We assume that photosynthetic processes utilise 5% of this absorbed energy, and the remainder is conducted into the surrounding ice. Since these cells are coloured by the purple purpurogallin pigment, we assume the reflective radiative forcing to be negligible, as demonstrated by Dial et al. (2018). We approximate the daily radiative forcing by multiplying the hourly instantaneous forcing by 3600 s h^{-1} and summing. Melt was then determined by scaling by 10^4 to convert m^2 to cm^2 and dividing by the latent heat of fusion for melting (334 J cm^{-3}). To calculate the percentage of daily melt caused by algal growth, we expressed the biological melting as a percentage of the mean ablative losses for the same day measured at a network of nine ablation stakes, converted into cm water equivalent using the ratio of density of ice (668 or 917 kg m^{-3}) to density of water (1000 kg m^{-3}). Two values were used for the density of ice, representing upper and lower bounds for local ice density resulting from weathering. These values were presented by Smith et al. (2017) based upon in-field measurements close to our field site during the same time of year. Using the upper value for ice density assumed the surface was composed of solid ice not weathered ice, making this a conservative estimate of biological contribution, whereas the lower value is more realistic for weathered summer ice in this area. Lower density ice represents a smaller water equivalent per unit surface lowering, such that the percentage accounted for by biological melting is greater.

2.87 UAV and Sentinel-2 remote-sensing

Having quantified algal melt acceleration in localised patches using the methods described in 2.2 – 2.6, we then used a multispectral camera mounted to a small UAV to quantify algal coverage across a $200 \times 200 \text{ m}$ area at our field site. UAV mapping took place over a ~~This~~ $200 \times 200 \text{ m}$ sample area that was kept pristine throughout the study period to minimise artefacts of our presence appearing in the UAV imagery. Inside the sampling area we placed fifteen $10 \times 10 \text{ cm}$ Ground Control points (GCPs) whose precise location was measured using a Trimble differential GPS. At these markers we

also made ground spectral measurements using an ASD-Field Spec Pro 3 immediately after each flight. The UAV itself was a Steadidrone Mavrik-M quadcopter onto which we integrated a MicaSense Red-Edge multispectral camera. The camera is sensitive in 5 discrete bands with center wavelenths 475, 560, 668, 717 and 840 nm, with bandwidths 20, 20, 10, 10, 40 nm respectively. The horizontal field of view was 47.2° and the focal length 5.4 mm.

We integrated a MicaSense Red-Edge multispectral camera onto a Steadidrone Mavrik-M quadcopter. The camera was remotely triggered through the autopilot which was programmed along with the flight coordinates in the open-source software Mission Planner (<http://ardupilot.org/planner/>). Multiband TIFF images were acquired at approximately 2 cm ground resolution with 60% overlap and 40% sidelap. The flights were less than 20 minutes long and at an altitude of 30 m above the ice surface.

We applied radiometric calibration and geometric distortion correction procedures to acquired imagery following MicaSense procedures (<https://support.micasense.com/hc/en-us/articles/115000351194-RedEdge-Camera-Radiometric-Calibration-Model> and https://github.com/atedstone/micasense_calibration). We then converted from radiance to reflectance using time-dependent regression between images of the MicaSense Calibrated Reflectance Panel acquired before and after each flight (i.e. a regression line was computed between the reflectance of the white reference panel at the start and end of the flight and used to quantify the change in irradiance during the flight). Finally, the individual reflectance-corrected images were mosaiced using AgiSoft PhotoScan following procedures developed by the USGS (<https://uas.usgs.gov/pdf/PhotoScanProcessingMicaSenseMar2017.pdf>), yielding a multi-spectral ortho-mosaic with 5 cm ground resolution, georectified to our GCPs. There was generally close agreement between the while the agreement between the ground, UAV and satellite-derived albedo is generally good although, there are some noticeable differences that we believe to be the result of different radiometric calibration techniques for satellite, UAV and ground measurements and the differing degrees of spatial integration that are quantified and discussed in a separate paper.

To upscale further, we used multispectral data from the Copernicus Sentinel-2 satellite. We selected the 100 x 100 km tile covering our field site (T22WEV) on the closest cloud-free day to our UAV flight on 21st July. The L1C product was downloaded from SentinelHub (Sinergise, Slovenia). The L1C product was processed to L2A using the ESA Sen2Cor command line tool (<http://step.esa.int/main/third-party-plugins-2/sen2cor/>), including atmopsheric correction and reprojection to 20 m resolution. The L2A product was then available for analysis as described in Section 2.8.

2.9 Sentinel-2 Data Processing

~~Sentinel-2 L1C data were downloaded from SentinelHub (Sinergise, Slovenia). The ESA Sen2Cor algorithm was used to convert the images to L2A (surface reflectance).~~

2.108 Supervised Classification Algorithms and albedo mapping

To map and quantify spatial coverage of algae over the ice-sheet surface we employed a novel-supervised classification scheme-wherein-. A RF-random forest classifier was trained on the field spectra collected on the ice surface (see section 2.3) and then applied to multispectral images gathered using athe UAV and the Sentinel-2 satellite. We also included spectra obtained at the same field site in July 2016 to out training set, giving a total of 231 individual labelled spectra. -A schematic of the classification workflow is provided in Supp Info 3. Our directional-reflectance measurementsHCRF measurements were first reduced to reflectance values at five key wavelengths coincident with the centre wavelengths measured by the MicaSense Red-Edge camera mounted to our UAV (blue: 0.475, green: 0.560, red: 0.668, red-edge: 0.717, NIR: 0.840 μm). A data table was produced with these five wavelengths as columns, and a separate row for each individual sample surface measured during our field spectroscopy. The reflectance at each wavelength was therefore a feature vector for the classifier. The classification labels were the surface type as determined by visual inspection: SN (snow), CI (clean ice), CC (cryoconite), WAT (water), L_{bio} (low biomass bloom) and H_{bio} (high biomass algal bloom). For the algal surface classes our visual assessment was corroborated with microscopy as described in section 2.2. This data table was then shuffled and split into a training set (780%) and a test set (230%). The training set was then used to train three individual supervised classification algorithms: Naive Bayes, K-nearest neighbours (KNN) and support vector machine (SVM). For the SVM, the parameters C and gamma were tuned using grid search cross validation. Two ensemble classifiers were also trained: a voting classifier that combined the predictions of each of the three individual classifiers, and a RERandom forest (RF) algorithm. The performance of each classifier was measured using precision, accuracy, recall and F1 score and also by plotting the confusion matrix and normalised confusion matrix for each classifier. In all cases the RF outperformed the other classifiers according to all available metrics (Supp Info 4). The performance of the RF classifier was thenfinally measured on the test set, demonstrating the algorithm's ability to generalise to unseen data outside of the training set. Overfitting is not usually associated with the RF classifier, and the strong performance on both our training and test sets _confirms that the model generalizes well. For these reasons, we used the RF algorithm to classify our multispectral UAV and Sentinel-2 images. Training the classifier using data from field spectroscopy ensures the quality of each labelled datapoint in the training set, since our sampling areas were homogenous and surface samples analysed in the laboratory, circumventing issues of spatial heterogeneity and uncertainty in labelling that could lead to ambiguity for direct labelling of aerial images. The RF algorithm was then applied to the processed UAV image.Simultaneously to the surface classification, we calculated the albedo in each pixel using the narrowband to broadband conversion of Knap et al. (2002) applied to the reflectance at each of the five bands.-

This protocol was then repeated for Sentinel-2 imagery. However, additional bands are available for use as feature vectors in the case of Sentinel-2. In that case the directional reflectance data was reduced to eight bands coincident with the centre wavelengths measured by Sentinel-2 at 20m ground resolution (0.480, 0.560, 0.665, 0.705, 0.740, 0.788, 0.865, 1.610 μm). Training on reduced hyperspectral data is a novel approach which has several advantages over gathering multispectral data: first, the method is sensor-agnostic because the classifier can be retrained with a different selection of wavelengths for other upscaling platforms, enhancing the reuseability of the field measurements; second, we have confidence in our labels because each sample has been laboratory analysed to confirm its composition, reducing label ambiguity; finally, the limited field of view of the field spectrometer reduces error arising from mixing of spectra from heterogeneous ice surfaces. Sentinel-2 imagery was masked using the MeASUREs Greenland Ice Mapping Project ice mask (<https://nsidc.org/data/nsidc-0714>) to eliminate non-ice areas from our spatial analyses. Pixels with more than 50% probability of being obscured by cloud were masked using the Sentinel-2 L2A cloud product generated by the Sen2Cor processor. Training the classifiers using data from field spectroscopy ensures the quality of each labelled datapoint in the training set. For the calculation of albedo in each pixel, the additional bands available in the Sentinel-2 images enabled the application of Liang et al.s (2002) narrowband to broadband conversion. The entire workflow was achieved using bespoke Python scripts that are available in our repository. For both the UAV and Sentinel classifiers, the final model are available in our data repository. All of the remote-sensing and supervised classification was achieved using bespoke Python scripts available in our repository.

2.4.19 Comparing 2016 and 2017 using MODIS

2017 was an especially bright year for the GrIS, whereas 2016 was especially dark. For this reason, we conducted a comparison between the algal coverage on the same dates in 2016 and 2017. First, we examined variations in the extent and duration of the Dark Zone along with snow depths and snow clearing dates for the south western ablation zone using MODIS, following the method of Tedstone et al. (2017). Dark ice extent and duration, and snow depths and clearing dates, were calculated after Tedstone et al. (2017), where full methods may be found. Bare-ice was mapped by applying a threshold reflectance value ($R < 0.60$ at 0.841-0.871 μm) to the MOD09GA Daily Land Surface Reflectance Collection 6 product. Within the bare-ice area, dark-ice was mapped using a lower reflectance threshold ($R < 0.45$ at 0.62 – 0.67 μm). The area of interest was the “common area” defined by Tedstone et al. (2017) bounded within the latitudinal range 65 – 70° N, and is equal to that used by Wang et al. (2019). To measure the annual dark-ice extent (in km^2) we counted the pixels that were dark for at least 5 days each year. The annual duration was defined at each pixel as the percentage of daily cloud-free observations made in each JJA period which were classified as dark. The timing of bare-ice appearance was calculated from MODIS using a rolling window approach on each pixel (see Tedstone et al. 2017). The mean snow depths were extracted from outputs from the regional climate model MAR v3.8 (Fettweis et al. 2016) run at 7.5 km resolution forced by ECMWF ERA-

495 Interim reanalysis data (Dee et al. 2011). These data enabled a comparison of the extent and timing of dark-ice in 2016 and
2017.

500 To examine algal coverage in each year we identified the Sentinel-2 tile covering our field site (22WEV) on the closest
cloud-free date to our UAV flight day (21st July) in each year. These were 28th July 2017 and 25th July 2016. The non-ice
areas were masked out using the MeASURES GIMP mask and the RF classifier described in Section 2.8 was applied to the
images to quantify coverage by each of our five surface classes. Since we are interested in the bare-ice zone, snow covered
pixels were omitted from the calculations.

505 ~~Briefly, we used the MOD09GA Daily Land Surface Reflectance Collection 6 product to map bare and dark ice in 2016 and~~
~~2017. The MOD09GA uses reflectance from Terra and sensor degradation has been accounted for in the Collection 6~~
~~product. We detected bare ice and then dark ice within bare ice areas by applying thresholds to reflectance values. For bare~~
~~ice we adopted $R_{0.841-0.871\ \mu m} < 0.60$. For dark ice we used $R_{0.62-0.67\ \mu m} < 0.45$. We used the common dark ice area~~
510 ~~defined by Tedstone et al. (2017) to define the spatial sampling area for comparing 2016 and 2017. Annual dark ice extent~~
~~corresponds to the extent (in km²) covered by the pixels within the common area which were dark for at least 5 days each~~
~~year. Annual duration was defined at each pixel in the common area as the percentage of daily cloud-free observations made~~
~~in each JJA period which were classified as dark and is thereby normalised for cloud cover. The timing of bare ice~~
~~appearance within the common area was calculated from MODIS data using a rolling-window approach on each pixel. Mean~~
515 ~~snow depths over the common area were extracted from outputs of the regional climate model MAR v3.8 (Fettweis et al.,~~
~~2016), run at 7.5 km resolution forced by ECMWF ERA-Interim reanalysis data (Dee et al., 2011). To determine spatial~~
~~coverage by each surface class in each year we identified those Sentinel-2 tiles that were cloud free and available on 21st July~~
~~+/- 3 days in 2016 and 2017. For direct comparisons between the two years only tiles that were available and cloud-free in~~
~~both years were used. The surface coverage counts were pooled from all available tiles in each year and the mean coverage~~
520 ~~assumed to be representative across the dark zone. In 2016, additional cloud-free tiles were available so for calculating the~~
~~2016 runoff an additional 2 tiles were included in the analysis.~~

2.120 Runoff Modelling

525 Runoff at the regional scale was calculated using van As et al.'s (2017) a SMB model forced with local automatic
weather station and MODIS albedo observations (van As et al., 2012; 2017). The model interpolates meteorological
and radiative measurements from three PROMICE automatic weather stations on the K-Transect (KAN_L, KAN_M
and KAN_U) and bins them into twenty 100 m elevation bands (0 to 2,000 m a.s.l.). Surface albedo is adjusted from

MODIS Terra MOD10A1 albedo and is averaged into the same 100 m elevation bins. For every one-hour time step, the model iteratively solves the surface energy balance for the surface temperature. If energy components cannot be balanced due to the 0 °C surface temperature limit, a surplus energy sink for melting of snow or ice is included. If surface temperature is greater than the melting point, the surplus energy is used for melting of snow or ice. When calculating turbulent heat fluxes, aerodynamic surface roughness for momentum was set to 0.02 and 1 mm for snow and ice, respectively (after van As et al. 2005; 2012; Smeets and Van den Broeke, 2008). We extrapolate modelled runoff across the south-western GrIS (65 – 70 ° N) by deriving the areas of each elevation bin using the Greenland Ice Mapping Project (GIMP) DEM (Howat et al., 2014) constrained to the latitude range defined in Fig 4 (following Tedstone et al., 2017). Total summer runoff from bare-ice was calculated by summing runoff in elevation bins that had mean daily albedo of less than 0.60. Total summer runoff from dark-ice only was calculated in the same way but using a 0.39 threshold. In van As et al.'s (2017) study they compared the performance of the model with independent observations and found the error to be negligible in the bare-ice zone.

To determine the algal contribution to runoff, we took the following approach: i) Take the percentage of total melting attributed to algal darkening predicted by the energy balance modelling described in Section 2.6 for L_{bio} and H_{bio} surfaces; ii) Calculate the runoff from dark-ice within the western ablation zone using van As's (2017) model; iii) multiply the runoff by the proportional coverage by algae ($H_{\text{bio}} + L_{\text{bio}}$) derived from our Sentinel-2 remote-sensing, assuming the spatial coverage in 22WEV to be representative across the south-western ablation zone, to estimate the runoff from all algal covered ice within the Dark Zone; iv) multiply the runoff from all algal covered ice by the melt attributed to algal darkening weighted by the relative proportions of H_{bio} and L_{bio} coverage calculated in our Sentinel-2 classification maps. As discussed later in this manuscript, the Sentinel-2 algal coverage estimate is conservative because it often fails to resolve H_{bio} surfaces and therefore provides a lower bound on the runoff attributed to algae. An upper bound was therefore also calculated by assuming the spatial coverage derived from our UAV remote-sensing – which can accurately distinguish L_{bio} and H_{bio} - surfaces is

representative of the south-western Dark Zone. We were thereby able to estimate upper and lower limits for the runoff attributed to algal growth on the south western ablation zone.

~~We multiplied the predicted runoff by the upper and lower estimates of melt attributed to algae from our radiative forcing experiments, weighted by the relative coverage determined in our remote sensing experiments. This provided an upper and lower estimate of the amount of melting attributed to biology.~~

3. Results and Discussion

3.1 Algae reduce ice albedo

Field measurements were made 38 km inland of the western margin of the GrIS (near Kangerlussuaq, Greenland) in July 2017 (Fig 1A, 3C). This site is within the GrIS Dark Zone, close to the IMAU Weather Station S6. The albedo of patches of the ice surface was measured using an ASD Field Spectrometer with a cosine collector, rotated to look upwards and downwards on the end of a 1.5 m horizontal tripod arm. These measurements were followed immediately by the physical removal of the upper 2 cm of the ice surface within the same patches. These ice samples were fixed in glutaraldehyde for mineral dust and algal cell identification and quantification via microscopy. ~~The ice surfaces we studied clustered into four classes depending upon the algal abundance measured in the melted ice samples: High algal abundance (H_{bio}), Low algal abundance (L_{bio}), Clean Ice (CI) and Snow (SN). The algal abundance in each class was as follows: $H_{bio} = 2.9 \times 10^4 \pm 2.01 \times 10^4$, $L_{bio} = 4.73 \times 10^3 \pm 2.57 \times 10^3$, $CI = 625 \pm 381$, $SN = 0 \pm 0$ (1 SD). These cell abundances were significantly different between the classes (one-way ANOVA, $F = 10.21$, $p = 3 \times 10^{-5}$) which Bonferroni-corrected t-tests indicated to be due to variance between all four groups. The dominant species of algae were *Mesotaenium bergrenii* and *Ancylonema nordenskioldii* (Fig 2+BB), confirming observations made by Stibal et al. (2017) and Williamson et al. (2018) in the same region. Their long, thin and approximately cylindrical morphology has been shown to be near-optimal for light absorption (Kirk, 1976). Samples were divided into the following distinct classes, based upon qualitative observations of algal abundance: High algal abundance (H_{bio}), Low algal abundance (L_{bio}), Clean Ice (CI) and Snow (SN). The measured algal cell abundance (in cells mL^{-1}) in each surface class was as follows: $H_{bio} = 2.9 \times 10^4 \pm 2.01 \times 10^4$, $L_{bio} = 4.73 \times 10^3 \pm 2.57 \times 10^3$, $CI = 625 \pm 381$, $SN = 0 \pm 0$. These cell abundances were significantly different between the classes (one-way ANOVA, $F = 10.21$, $p = 3 \times 10^{-5}$) which Bonferroni-corrected t-tests indicated to be due to variance between all four groups.~~

The albedo of the ice surface also varied significantly between the surface classes (one-way ANOVA for broadband

albedo: $F = 7.9$, $p = 2.8 \times 10^{-4}$; spectrally-resolved ANOVA shown in Supp-Info-1F), again with Bonferroni-corrected t-tests showing variance between all four groups (Supp Info 45 C,D). Greater algal abundance was associated with lower albedo, with the albedo reduction concentrated in the visible wavelengths (Fig 24C) where both solar energy receipt and algal absorption peak (Fig 2A; Cook et al., 2017b; Williamson et al., 2018), diminishing towards longer near infra-red (NIR: $> 0.70 \mu\text{m}$) wavelengths where ice absorption, represented by the effective grain size, is most likely to cause albedo differences (Warren, 1982). A strong inverse correlation (Pearson's $R = 0.75$, $p = 2.74 \times 10^{-9}$) was observed between the natural logarithm of algal cell abundance (cells mL^{-1}) in the surface ice samples and broadband albedo (Fig 24D). The linear regression coefficient of determination between the albedo and the natural logarithm of cell abundance was 0.567, which is unsurprising since, it is unsurprising that the cell abundance does not account for all of the variation in albedo because there are also albedo-reducing effects related to the physical structure of the ice and presence of melt water also plays a primary role in controlling albedo independent of any light absorbing impurities (as demonstrated for snow by, for example, Warren, 1982). An inverse relationship was also observed between broadband albedo and biovolume (calculated as the sum of the products of the mean measured cell volumes and the cell counts for each algal species) but the coefficient of determination was lower ($r^2 = 0.42$). This may well be the result of larger cells having a smaller effect on albedo than more numerous, smaller cells for a given total volume. The relationship between absorption and scattering coefficients and cell size may also not be straightforward for algal cells due to an increasingly important contribution to the cell optical properties from internal heterogeneity, organelles, cell walls and the pigment packaging effect in larger cells (Morel and Bricaud, 1981; Haardt and Maske, 1987).

The albedo of H_{bio} and L_{bio} surfaces is depressed in the visible wavelengths ($0.40 - 0.70 \mu\text{m}$, Fig 22A), creating a 'red-edge' spectrum commonly used in other environments as a marker for photosynthetic pigments (Seager et al., 2005) and for mapping algae over the GrIS by Wang et al. (2018). Chlorophyll has a specific absorption feature at $0.68 \mu\text{m}$ which is hard to discern in the raw spectra, but clear in the derivative spectra (Fig 32A) for H_{bio} and L_{bio} but not CI and SN. This feature has previously been described as 'uniquely biological' (Painter et al., 2001) and supports the hypothesis that the albedo reduction observed in these samples is primarily due to algae. Our measurements therefore strongly indicate a biological role in reducing the albedo of the GrIS surface; however to test that the lower broadband and spectral (Fig 1C)-albedo (Fig 2C) observed on algal surfaces is primarily due to the presence of algal cells, it was also necessary to compare the albedo-reducing effects of the algae to that of local mineral dust:

3.2 Algae have greater impact on albedo than mineral dust

We used radiative transfer modelling to compare the albedo-reducing effects of local mineral particles and algal cells (Fig 3B). The model BioSNICAR_GO was used, which uses Mie theory to model the optical properties of mineral dusts, geometric optics to model the optical properties of ice grains and algal cells (whose dimensions far exceed the upper limit of

630 the Mie scattering domain) and a two stream radiative transfer code (Flanner et al., 2007; Cook et al. 2017). To compare
algal and mineral albedo-reducing effects, the model was run with fixed irradiance and ice physical properties that
were chosen to reduce the absolute error between the simulated albedo for ice without any impurities and our mean
measured clean ice spectrum and: the optical properties of local mineral dust and algal cells were used to incorporated each
of these impurities into the model individually.

635 To determine the optical properties of the mineral dust, organic matter was chemically removed from field samples and the
spectral reflectance of the cleaned minerals was measured using a spectrometer and integrating sphere, providing a target
spectrum for the DISORT radiative transfer model, thereby enabling the spectral complex refractive index of the minerals
(Fig 2 B) to be estimated following Skiles et al., (2017). Given the measured mineral dust particle size distribution (PSD;
640 Supp Info 1E), this enabled the optical properties of the bulk mixture of mineral dust to be calculated using Mie theory. The
minerals were much more reflective than those measured by Skiles et al. (2017) from snow in Colorado. The imaginary
refractive index of the mineral dust sample (Fig 3C) was lower than Skiles et al's (2017) dust samples and the other dust
samples included in our sensitivity study, indicating a greater prevalence of weakly absorbing minerals and scarcity of red
minerals in the bare-ice. The mass absorption coefficient, asymmetry parameter and single scattering albedo (Fig 4 B, C, D)
645 were broadly comparable to those of Skiles et al.'s (2017) finest dust sample which had a log-normal PSD with diameters
ranging between 0.1 and 1 μm (that sample was identical to the dust sample F1 included in this study). The majority of the
mineral mass in the field sample was made up composed of very small particles (Fig 4A), and an optically thick layer of
the minerals had a near-white colour to the naked eye. While the mean diameter was 1.86 μm , this was influenced by the
presence of infrequent a few very large fragments. 75% of the particles had diameter < 1.68 μm , and 50% had
650 diameter < 0.56 μm .

The optical properties of glacier algae were calculated using empirical measurements of pigment mass fractions from field
samples, an empirically derived absorption spectrum for the purpurogallin-like phenolic pigment, a pigment mixing model
(adapted from Cook et al. 2017a,b), a measured size distribution and a geometrical optics code that assumes chains of cells
to be circular cylinders, after Lee and Pilon (2013).

655 The effect of adding these local mineral dust to a simulated ice column varied depending upon the dust sample used (Fig
3B). For example, adding a hypothetical 300 $\mu\text{g/g}$ of mineral dust to the upper 1 mm of ice caused a small increase in albedo
(0.008) relative to clean ice. This was also the case for dusts F1 and F2, which caused an albedo increase of 0.01 and 0.002
respectively. The same mass mixing ratio of the P1, P2 and P3 dusts caused a small albedo reduction: 0.0005 (P1), 0.003
660 (P2) and 0.01 (P3). In contrast, adding 300 $\mu\text{g/g}$ of algae decreased the albedo by 0.02, was a small increase in broadband
albedo (Fig 2C). In contrast, adding algal cells to the simulated ice caused an albedo reduction due to the enhanced
absorption of incident light in the visible wavelengths. For example, adding a hypothetical 300 $\mu\text{g/g}$ mineral dust increased the ice broadband
albedo by 0.02, whereas the same mass mixing ratio of algal cells decreased the broadband albedo by 0.03. We present the albedo change resulting from 100, 300 and

500 ug/g mixing ratios of all the dust species and glacier algae in our sensitivity study in Table 1. There was no scenario where the addition of glacier algae could increase the albedo of the ice, and their albedo reducing effect always increased with additional biomass. The albedo reduction due to hematite-rich mineral dusts is concentrated into the shorter VIS wavelengths, as it is for algae. However, the spectral shape of ice with dust differs from ice with algae. For hematite-rich dust, the ice albedo increases with wavelength up to 0.70 μm ; for algae, the spectrum is much flatter or even downsloping with increasing wavelength between 0.35 and 0.45 μm before rising steeply to the “chlorophyll bump” at 0.55 μm , and a gentle increase to 0.70 μm . These spectral features are consistent with our field spectra for algal ice, and can only be recreated in the radiative transfer model when algal particles make up the majority of the surface impurity load.

This mass mixing ratio was chosen to be within the range of cell masses measured in our field samples for algal ice with the cells concentrated into the upper 1 mm of ice to match our observations. The increase in albedo caused by the addition of mineral dust may seem like a surprising result, but the ice itself had a relatively low albedo due to having a long absorbing path length (our simulated ice column had ice grains with diameter 3 – 10 mm) and the local mineral dust particles were sufficiently small, weakly absorbing and strongly scattering that their overall effect was to increase the light scattered skywards by the ice. In simulations with smaller ice grain radii (400 μm radii snow grains) and therefore higher initial albedo, the addition of 300 $\mu\text{g/g}$ mineral dust had negligible effect (< 0.001) whereas 300 $\mu\text{g/g}$ algae still reduced the albedo by > 0.02 . These radiative transfer simulations indicate that mineral dust is unlikely to be directly causing the albedo decline on the GrIS, although they may influence the ice albedo indirectly by acting as substrates for the formation of low-albedo microbial-mineral aggregates known as cryoconite granules, which are often found in quasi-cylindrical melt holes or scattered over ice surfaces (Wharton et al. 1985; Cook et al. 2015a) or by providing a nutrient source stimulating algal growth (Stibal et al. 2017). This is especially true because there is evidence in the previous literature that the dust present on the GrIS bare-ice surface are likely derived from a local source with no contribution from Asian dusts or volcanic ash (Wientjes et al. 2011) and that red minerals such as hematite, goethite and ilmenite are present only in very low concentrations (Wientjes et al. 2011; Tedesco et al. 2013; Sanna and Romeo, 2018) that would have a negligible effect on the ice optics. This was also supported by our preliminary mineralogical analysis of our local dust samples, implying that the minerals included in our sensitivity test are truly extreme upper end-members for albedo reduction and ‘redness’ caused by dust deposition in this region, and that mineral dusts are not responsible for albedo decline on the south-western GrIS.

These minimal direct albedo reducing effect from local minerals on the ice surface is seemingly in contrast to some previous studies such as Wientjes et al. (2010; 2011) and Bøggild (2010); however, we point out that neither of the Wientjes et al. (2010; 2011) studies directly measured the surface albedo or any optical properties of the mineral dusts retrieved from their GrIS sampling sites and only inferred mineralogical darkening from low spectral resolution MODIS data that did not consider biological darkening as a potential explanation for the suppressed albedo in the

visible wavelengths and the presence of a “wavy pattern” observed in across the dark zone in MODIS imagery. We argue that while the “wavy pattern” may be indicative of geological outcropping onto the ablation zone, it does not necessarily follow that these minerals are responsible for surface darkening, but perhaps act as stimuli for biological growth in-situ. In support of this, Wientjes et al. (2011) found strongly scattering and weakly absorbing quartz to be the dominant mineral in surface ice and speculated that biota may be having a darkening effect. Bøggild et al. (2010) found mineral dust to be an albedo reducer in Kronprinz Christian’s Land (80N, 24W) but this area is geologically and climatologically distinct from our field site, and their transect only spanned ~8 km from the ice-sheet margin, being an area prone to local dust deposition and not thought to be part of the “Dark Zone” proper. The mineral dust may provide a source of nutrients and shelter for glacier algae, making the mineral dust an enabler of biological albedo decline and exacerbating the so-called “wavy pattern” (Wientjes et al. (2011) created by outcropping dusts. In contrast this study, we have demonstrated using empirical measurements and radiative transfer modelling that algae are potent albedo reducers and mineral dusts are not, at least in this region where small, strongly scattering and weakly absorbing mineral fragments sit atop relatively dark bare-ice. These findings are consistent with several previous studies (Stibal et al. 2017; Yallop et al. 2012) that found mineral dust to be insignificant for explaining albedo variations in the same region; or that algal cells had a greater albedo reducing effect than mineral dusts in north-west Greenland (Aoki et al. 2011).

3.3 Indirect effects of algae

Algae predominantly reduce the ice albedo in the visible wavelengths (0.40 – 0.70 μm), whereas variations in the NIR result mainly from changes to ice grain radii and the presence of liquid water (Warren, 1982; Green et al., 2002). We compared the area of an absorption feature (i.e. the sum of the distances between a straight line drawn between the shoulders – 0.95 μm and 1.035 μm - of the absorption feature and the albedo at each wavelength) centered at 1.032 μm between the different surface types, finding significant differences between all four surface classes (one-way ANOVA, $F = 12.8$, $p = 7.16 \times 10^{-7}$) driven predominantly by variations between the two algal surfaces and the two clean surfaces. This absorption feature is linked to the optical properties of snow because it scales with grain size (Nolin and Dozier, 2000), so we interpret these variations as evidence that the optical properties of the ice surface differed between the surface classes, having an effect on the measured albedo. The feature area is smallest for H_{bio} followed by L_{bio} , CI and largest for SN (Supp Info 4B, Supp Info 3). The features with the smaller areas also had lower albedo minima. The absorption features are also subtly, but systematically, left-asymmetric for the algal surfaces, consistent with the presence of liquid water in the fast-melting ice beneath algal blooms (Green et al., 1998; Cook et al., 2017b). These observations, along with the linear regression coefficient of determination of 0.57 between albedo and the natural logarithm of cell abundance suggest that the lower albedo of algal surfaces is not explained entirely by enhanced absorption due to algae, but also due to the smoother, wetter ice surface with fewer opportunities for high-angle

scattering of photons, compared to the well-drained and porous CI surfaces. The spatial and temporal development of the weathering crust is therefore a major control on bare-ice albedo. Cause and effect is unclear because algae may cause this by enhancing melting of the weathered surface or may grow preferentially where there is already more melt. We expect the explanation to be a combination of these two interlinked processes, especially since melting of ice liberates nutrients that stimulate algal growth. Our radiative transfer model also indicates that enhanced absorption of solar radiation at the ice surface due to glacier algae also reduces the energy penetrating into the ice and causing internal erosion, while downwards melting at the surface is enhanced due to emission of absorbed solar energy as heat, promoting thinner, less porous weathering crusts with more interstitial water and feeding back to lower albedo underlying ice. ThisWe therefore supportshighlight the role of indirect feedbacks (Cook et al., 2017a,b; Tuzet et al., 2019) in biological darkening of ice-sheets. This process is self-amplifying because algal growth is stimulated by melt, which can be enhanced by algal growth (Yallop et al., 2012; Ganey et al., 2017; Stibal et al., 2017; Cook et al., 2017a,b; Dial et al., 2018), enhancing the albedo lowering process: - an example of a biocryomorphic process where biota alter the physical, chemical and hydrological conditions of the ice surface with beneficial consequences to the biota (Cook et al. 2015b).

3.4 Algae enhance radiative forcing and melt

Having determined that glacierice algae reduce the ice surface albedo, we took an empirical approach to quantifying their impact upon energy balance following Ganey et al. (2017), which includes both direct albedo effects (enhanced absorption of shortwave solar radiation by the algal cells) and the indirect effects explained above. We used the product of the difference in spectral albedo between algal and clean ice surfaces and the incoming spectral irradiance to calculate the hourly radiative forcing (RF) of algae, assuming mineral dust is not causing significant albedo reduction. Integrated over the entire day, this indicated a daily mean biological RFradiative forcing of 116 W m^{-2} and 65 W m^{-2} for H_{bio} and L_{bio} surfaces respectively, similar to RFs for Alaskan snow algae calculated by Ganey et al (2017). We used the biological radiative forcing integrated over the entire day (Supp Info 5A) and the latent heat of fusion for ice (334 J cm^{-3}) to estimate 1.35 ± 0.01 (S.E) cm w.e. ofprovide an estimate of melting due to algae under the assumption that the cold content of the ice is depleted (i.e. ice is at 0°C). We made two calculations with ice densities 917 kg m^{-3} (solid ice) and 668 kg m^{-3} (weathered ice) following Smith et al (2017), providing upper and lower bounds for melt attributed to algae depending upon local ice density. The melting due to algae in H_{bio} areas on 21st July, was estimated to be 1.3 to 1.9 cm w.e. in H_{bio} areas, which represents between 21 and 29% of the total melting measured across a network of ablation stakes at our site (6.8 cm). For L_{bio} sites, biological melting on 21st July 2017 was 0.76 to 1.071.01 \pm 0.01 (S.E) cm w.e., which corresponds to between 12 and 18% of the observed ablation. We corroborated this estimate using a point surface energy balance model (Brock and Arnold et al. 2000).

The melt attributed to the presence of algae predicted by the energy balance modelling method was similar to that predicted using the radiative forcing method, with 1.37 ± 0.48 (S.E) cm w.e. attributed to H_{bio} and 0.95 ± 0.41 (S.E) cm w.e. attributed to L_{bio} . Expressing the melt attributed to algae as a proportion of the total melting in the algal sites gives 26.15 ± 3.77 % (S.E) of the local melting attributed to algae in the H_{bio} surfaces and 21.62 ± 5.07 % (S.E) for L_{bio} surfaces.

These estimates are similar to those made by Ganey et al. (2017) for heavy algal blooms on snow (21% of total melt due to ablation):

3.5 Algae cover a large proportion of the ice sheet are widespread across the south-western ablation zone

Our analyses demonstrate that algae have a dramatic darkening effect on the ice surface, leading to increased melting. However, the importance of this effect depends upon the spatial extent of the algal blooms over thousands of kilometers. We made 146 directional reflectance measurements immediately after albedo measurements for each sample surface, providing training data for supervised classification algorithms that were applied to multispectral imagery obtained by a UAV. Directional reflectance is a more appropriate measurement than albedo for this purpose because it better approximates the measurements made by orbital remote sensing platforms and are less affected by surface heterogeneity, having smaller viewing footprints. Our ground spectra were reduced to five bands matching the centre wavelengths measured by our UAV multispectral camera. The reflectance dataset was divided randomly into training (80%) and test (20%) sets. This data was then used to train a random forest algorithm (chosen because of its high performance relative to other classifiers) to predict the surface class for each pixel in our UAV image, thereby enabling spatial upscaling of our field spectroscopic measurements. The accuracy, precision, recall and F1 score of the random forest classifier on the test set were all 95%.

The UAV image was obtained by flying a MicaSense Red-Edge camera integrated onto a quadcopter over a 0.04 km^2 area grid with a ground resolution of 5 cm at our field site on 21st July 2017. To determine spatial coverage at our field site we applied an RF classifier trained on our HCRF measurements, to multispectral images acquired from a UAV flown over a $200 \times 200 \text{ m}$ area. The classified UAV image indicated that 78.5% of the area was covered by algal blooms of which 61.1%

800 was L_{bio} and 17.4% was H_{bio} (Table 23; Figure 35). The high ground resolution of the imagery enabled a qualitative assessment of the algorithm performance by visual comparison between the classifier and the raw imagery (following Ryan et al. 2018a). The algorithm produced qualitatively realistic bloom shapes, correctly placed water in channels and individual cryoconite holes in their correct positions. The confusion matrix indicates that occasional misclassifications are generally between water and cryoconite (Supp Info 26). This is unsurprising since both
805 cryoconite and water have relatively flat spectral shapes with few spectral features and cryoconite is often found beneath pools of surface water. We also point out that our cryoconite spectral reflectance measurements were made with cryoconite filling the entire field of view of the spectrometer, so best represent large cryoconite holes or dispersed cryoconite rather than surfaces peppered with many small holes. There was also some ambiguity between thin, wet snow and bare glacier ice, as these surfaces are spectrally similar. Nevertheless, these misclassifications affect a small
810 area of the pixel and do not affect our estimate of algal bloom coverage.

~~An RF training set was classifier was also trained for application to then produced for application to Sentinel-2 satellite data by reducing the hyperspectral ground data to nine bands, coincident with those measured by Sentinel-2 at 20 m ground resolution (Fig 5). The confusion matrices (Supp Info 26) indicate similar misclassification types and frequencies to the~~
815 ~~UAV model. The RF model was applied to the Sentinel-2 tiles that were within the Dark Zone, covering our field site on the closest cloud-free and available on the date of retrieval to our UAV flight +/- 3 days. Non-ice areas were masked out prior to analyses. The classifier then predicted the surface type pixelwise across all the Sentinel-2 100 x 100 km tiles. The resulting data were then pooled into one large dataset. The mean predicted algal coverage across all tiles was 1858.87%; however there was significant spatial heterogeneity, with the tile covering our field site in the Kangerlussuaq region having~~
820 ~~44% algal coverage. H_{bio} surfaces were much less common than L_{bio} ($H_{\text{bio}} \equiv 2.53\%$, $L_{\text{bio}} \equiv 56.54\%$, Table 23). The spatial coverage by algae was different in the Sentinel and UAV datasets especially for H_{bio} , likely because a) the Sentinel-2 imagery includes ice that is outside of the Dark Zone, raising the overall reflectivity, and b) even in the UAV image, which was retrieved from within the Dark Zone, H_{bio} surfaces comprise just 157% of the ice surface and have a patchy distribution, meaning they may not be detected by the 20 m resolution Sentinel-2 data. The lowest albedo~~
825 ~~surfaces – cryoconite and water – cover a small fraction (< 3%) of the total area in both UAV and Sentinel-2 images (Table 23), although we note that many individual cryoconite holes will not be detected due to being smaller than the spatial resolution of either Sentinel-2 or the UAV. The spatial coverages reported here from our multispectral UAV imagery are consistent with a k-nearest neighbours classification scheme applied to RGB (Red, Green, Blue) imagery from a fixed wing UAV flight over the Kangerlussuaq region by Ryan et al. (2018a). They found up to 85% of the ice surface to be composed of ‘ice containing uniformly distributed impurities’ in the same region of the Dark Zone in July 2014, which our observations confirm were dominated by algae. They also found < 2% of the ice surface to be cryoconite covered and water coverage was < 5% (except for a supraglacial lake in their imaged area). This analysis demonstrates that algae are a major component of the ice surface. The larger spatial coverage observed in UAV images~~

compared to Sentinel-2 images likely results from spatial integration occurring at the coarser spatial resolution associated with Sentinel-2 data, where pixels are likely to be classified as CI unless the majority of the pixel is algae-covered. Smaller H_{bio} patches are rarely detected because they are very unlikely to cover the majority of a 20 m pixel. The higher detection limit for algae with decreasing ground resolution makes our estimate of spatial coverage from Sentinel-2 conservative. We point out that this will have a much larger effect on studies aiming to quantify cell abundance using Sentinel-3 where the ground resolution is 300 m.

3.6 Algae reduce ice sheet the ice albedo at the landscape scale across the south-western ablation zone

Multispectral imagery acquired by the UAV was converted to albedo using the narrowband to broadband conversion of Knap et al. (1998). The additional bands for the Sentinel-2 data enabled the application of Liang et al.'s (2002) narrowband to broadband conversion. There was a significant difference between the albedos of each surface class in all four datasets, consistent with the findings from our ground spectroscopy (Figure 35; Table 42). The albedo of each surface class is approximately consistent between the datasets, despite the variation in spatial coverage (Table 2), giving confidence in the accuracy of our remote-sensing albedo retrievals and the classification algorithm.

Our satellite remote-sensing data demonstrates that algal blooms are a major component of the ice surface in this area (Table 42, Figure 3, Supp-Info 4), and in the expansive areas (Fig 5) where where they algae are present the ice albedo is on average 0.13 lower for L_{bio} and 0.205 lower for H_{bio} compared to clean ice (Table 42). This, combined with our ground-based spectroscopy and radiative forcing calculations, radiative forcing calculations, radiative transfer and energy balance modelling, provides robust evidence in support of algae having a significant melt-accelerating effect on the GrIS. We cannot yet explicitly separate mineral and biological effects, but our theoretical and empirical analyses indicate that: a) local mineral dust cannot explain the observed albedo reduction, b) low-albedo areas had significantly elevated algal cell numbers relative to clean ice, c) uniquely biological features were detectable in the spectra and derivative spectra for the lower albedo sites, and d) radiative transfer models incorporating algal cells with realistic pigment profiles demonstrate the mechanism of albedo reduction. These reasons observations confirm that supervised classification of H_{bio} and L_{bio} surfaces is indeed detecting surfaces with high algal loading and can be used to make a conservative estimate of algal bloom extent. Again, we point out that this estimate is conservative because there is certain to be ice algae present in low numbers in some of the areas that are classified as clean, and H_{bio} patches are not detected where the area of the patch is much smaller than the ground resolution of the sensor. Furthermore, these calculations consider the total albedo-reducing effect, inclusive of ice structure and meltwater feedbacks, not only the direct light-absorbing effects of the algal biomass.

3.7 Algae cause enhanced GrIS runoff

870

875

We ran a surface mass balance (SMB) model forced with local automatic weather station and MODIS albedo observations (van As et al., 2012) to estimate 45.5 Gt runoff from all bare-ice and 33.8 Gt from dark-ice in 2017. We used the mean spatial coverage determined using our remote-sensing in each year and our radiative forcing calculations that attributed 21.62 ± 5.07 (SE) % of melting to algae in L_{bio} sites and 26.15 ± 3.77 (SE) % in H_{bio} sites to generate estimates for the GrIS runoff caused by algal growth. We have provided upper and lower estimates based on our two remote-sensing datasets, because while our UAV is able to accurately map H_{bio} and L_{bio} surfaces, we cannot be completely sure that the spatial coverage derived from the 200 x 200 m area is representative of the south-western Dark Zone. At the same time, our Sentinel-2 remote-sensing underestimates algal coverage because H_{bio} patches are often too small to be resolved at 20 m pixel resolution. Therefore, we used the spatial coverage determined by our Sentinel-2 classification as a lower bound, and spatial coverage determined by our UAV classification as an upper bound on our estimate of total runoff attributed to the presence of algae.

880

885

We found that in 2017 between 4.4 – 6.0 Gt of ice loss could be attributed to the growth of algae, representing 10 - 13 % of the total runoff from the south-western GrIS, with the lower estimate generated using algal coverage from Sentinel-2 and the upper estimate generated using spatial coverage at our field site from our UAV. When the the calculations to runoff were restricted to the Dark Zone only (i.e. excluding areas in the ablation zone not classified as “dark”) algal contributions to total runoff were up to 18 %. These calculations confirm that algal growth is an important factor in the contribution of the GrIS to global sea level rise. This contribution will increase if biologically-darkened areas expand or a greater proportion of the ice is covered by high biomass blooms under warmer climates. These observations therefore indicate that the omission of biological growth is leading current models to underestimate future GrIS contributions to sea level rise.

3.78 Interannual variability and potential positive feedback Enhanced algal albedo reduction in a ‘dark-year’

890

895

Satellite remote sensing using MODIS data (Figure 46) indicates that 2017 was a particularly high albedo year; where the Dark Zone was both especially smaller and brighter than in previous years, whereas 2016 was a particularly low-albedo year where the dark zone was wider and darker than most years. Figure 4 (A,B) shows the dark ice extent and duration for 2016 and 2017 (extending the time series of Tedstone et al., 2017) – 2016 was a year of exceptional dark ice extent and duration, while 2017 had half the dark ice extent and a much shorter duration (Fig 6 A,B and Tedstone et al. 2017). Figure 4C,D shows that summer 2016 was preceded by much thinner snow, which melted away to reveal bare ice over a month earlier than in 2017. Furthermore, there were several additional snowfall events (5-10 cm snow) during our field work period in 2017, which did not occur in the same period during 2016. Previous field evidence (Williamson et al., 2018) demonstrates that the ice was darkened by high concentrations of algae in 2016. We therefore applied our classification algorithms to Sentinel-2 data from the same date and precisely the same locations for both 2016 and for 2017 (Figure 3, Table 1, Table 2, Supp Info 4). In our Sentinel-2 remote-sensing tile (22WEV) the bare-ice zone was wider in 2016 (6758

900
905
910
915
920
925
930

km²) than in 2017 (6205 km²), and a larger area was covered with algae (on 25th July 2016, 3919 km² was covered by algae compared to 3653 km² on 28th July 2017). While the proportional total algal coverage was similar between the two years (57.99 % in 2016, 58.87 % in 2017), the proportion of the algal ice that was classified H_{bio} was much higher in 2016 (8.35 %) compared to 2017 (2.54 %). The mean albedos and their standard deviations were very similar for each ice surface class in both years (Table 2). The runoff from the south-western GrIS bare-ice (albedo < 0.6) was 94.1 Gt in 2016, of which 67.6 was from dark-ice (albedo < 0.39). We estimate that 8.7 – 12.2 Gt of this runoff was attributable to the growth of algae, representing 9 – 13 % of the total runoff from bare-ice runoff. The absolute values for runoff are therefore much higher but the proportion of the bare-ice total attributed to algae approximately the same between the two years.

The snow line had retreated further, faster in 2016 compared to 2017 creating a wider bare-ice zone that had existed for longer and was not recovered by summer snowfall events, whereas in 2017 a smaller bare-ice was exposed later and was recovered by 5 - 10 cm of snow several times during the summer (Fig 6 C, D). The more prolonged exposure of a larger bare-ice zone in 2016 enabled L_{bio} surfaces to extend to higher elevations and biomass to accumulate to greater mass concentrations at lower elevations in summer 2016, explaining the greater H_{bio} coverage. This indicates that the intensity of the algal bloom is a function of exposure time, as postulated by Tedstone et al. (2017) and Williamson et al. (2018). More prolonged exposure of larger ablation areas under a warming climate (Stroeve et al. 2013; Shimada et al. 2016; Tedesco et al. 2016; Tedstone et al. 2017) are likely to be prone to more spatially expansive, darker algal blooms that enhance melt rates, leading to a potential positive feedback that is not currently accounted for in surface mass balance models whereby earlier exposure of bare-ice leads to enhanced algal coverage, more of which will be able to accumulate higher biomass, and accelerate melting. Melting, in turn stimulates algal growth by liberating nutrients and liquid water. There was a much larger spatial coverage by algae in 2016 than 2017 (total algal coverage = 61% in 2016, 18% in 2017 for the same areas) and a larger proportion of H_{bio} (9% in 2016 compared to 4% in 2017). The mean albedos for the algal surfaces were lower in 2016 than 2017 but very similar for all other surface types. This indicates that the ice surface was indeed enhanced by greater spatial coverage of algal blooms with either greater biomass or pigmentation in 2016 compared to 2017. The snow line had retreated further, faster in 2016 compared to 2017 creating a wider bare ice zone that had existed for longer at the time of our remote sensing (Supp Info 4). Interestingly, the L_{bio} coverage extends further inland in the darker year, whereas H_{bio} surface extend further towards the margin. This suggests that newly exposed ice at higher elevations was colonised by relatively low abundance blooms, whereas heavier blooms developed on ice at lower elevations that was exposed for longer. This suggests the intensity of the algal bloom is a function of exposure time (Tedstone et al., 2017) and corroborates the findings of space-for-time experiments by Williamson et al. (2018). Therefore, the 2016 dark year was indeed especially low albedo due to particularly extensive and intense algal blooming on the GrIS surface, enabled by prolonged bare-ice exposure. This interannual comparison demonstrates that more prolonged exposure of larger ablation areas under a warming climate (Stroeve et al. 2013; Shimada et al. 2016; Tedesco et al. 2016; Tedstone et al. 2017) are likely to be prone to more spatially expansive, darker algal blooms that enhance melt rates, leading to a potential positive feedback that is not currently

accounted for in surface mass balance models. The existence of a bright area at the edge of the ablation zone may seem to undermine exposure time as a driver of algal growth; however, we do not discount the importance of outcropping mineral dusts from stratified ice layers which may well be critical nutrient stimuli for glacier algae which then darken the ice surface (Stibal et al. 2017). The emergence of these minerals may impose a lower boundary on the dark zone, or alternatively the melt runoff and/or surface slope at lower elevations may be sufficient to wash light-absorbing particles off the ice surface at these very low elevations.

~~These observations therefore indicate that the omission of biological growth is leading current models to underestimate future GrIS contributions to sea level rise.~~

3.8 Algae cause enhanced GrIS runoff

We ran a surface mass balance (SMB) model forced with local automatic weather station and MODIS albedo observations (van As et al., 2012) to estimate 94.1 Gt of runoff from bare ice on the western GrIS (albedo < 0.6) and 67.6 Gt runoff from dark ice (albedo < 0.39) within the latitudinal range defined in Fig. 4. We used the mean spatial coverage determined using our remote sensing in each year and our radiative forcing calculations that attributed 12-18% of melting to algae in L_{bio} sites and 21-29% in H_{bio} sites to generate upper and lower estimates for the GrIS runoff caused by algal growth.

We found that in 2017 between 0.08–0.11 Gt of ice loss could be attributed to the growth of algae, representing 1–2% of the total runoff from the western GrIS. In 2016 this contribution increased to 5.5–8.0 Gt, representing 6–9% of the total runoff from the western GrIS. These calculations confirm that algal growth is an important factor in contribution of the GrIS to global sea level rise. The interannual comparison strongly indicates that this contribution will increase if biologically-darkened areas expand or a greater proportion of the ice is covered by high biomass blooms under warmer climates.

4. Conclusions

Our measurements and modelling demonstrate that the growth of algae on the GrIS is accelerating the rate of melting and increasing the GrIS contribution to global sea level rise. Our field spectra show a dramatic depression of the surface albedo in the visible wavelengths for surfaces contaminated by algae. Derivative analysis of the same spectra show “uniquely biological” absorption features and an inverse relationship was observed between biomass and surface albedo. We employ a novel radiative transfer model to show that this albedo decline cannot be attributed to local mineral dusts. Radiative forcing calculations and an energy balance model predict that melting of glacier ice can be accelerated by 21.62 ± 5.07 (SE) % for L_{bio} surfaces and 26.15 ± 3.77 (SE) % for H_{bio} surfaces. We demonstrate that the growth of algae occurs over a large proportion of the ablating area of the south western GrIS by training a RFRandom forest classifier to identify algal blooms in remote-sensing data from a UAV and Sentinel 2, finding 78.5 % of the surface within a 200 x 200 m sample area at our field site to be algae covered. Using Sentinel-2 we detected algae covering

57.99 % of the Kangerlussuaq region in 2017 and 58.87 % of the same region in 2016, although we point out that the spatial resolution of the sensor makes these conservative estimates, especially for H_{bio} surfaces. ~~In the particularly dark 2016 melt season, coverage by algae was much higher than in the bright 2017 melt season. Runoff modelling informed by our field measurements and remote-sensing estimate between 4.4 and 6.0 Gt of runoff from the south western ablation zone could be attributed to the growth of algae in summer 2017, representing 10- 13% of the total. Because 2017 was a particularly high albedo year for the south western GrIS, we also ran our analysis for the particularly low-albedo 2016 melt season. In 2016 a wider bare-ice zone was exposed for longer, and there was a concomitant increase in the extent of the algal bloom, more of which was classified as H_{bio} (high biomass). The percentage algal contribution to south western GrIS runoff was approximately the same as in 2017 (9 – 13 %) but the absolute volume was much higher (7.3 – 11.9 Gt). This interannual comparison indicates the existence of a feedback because in years where snow retreats further, faster, there is a larger and more prolonged area for algal bloom development where melting is enhanced, stimulating further algal growth. Our field measurements and remote sensing data inform a runoff model that estimates 5.5 – 8.0 Gt or 6-9 % of the total runoff in summer 2016 could be attributed to the growth of algae. This study therefore unequivocally demonstrates that algae are important albedo-reducers and cause a melt-enhancing feedback across the south-western GrIS. The omission of these critical biological albedo feedbacks from predictive models of GrIS runoff is leading to underestimation of future ice mass loss and contribution to global sea level rise. This is particularly significant because larger ablation zones and longer growth seasons are expected in a future warmer climate.~~

5 Data Availability

Codes and datasets used in this study are available at the following doi's:

BioSNICAR_GO code and data: DOI: 10.5281/zenodo.2598041

Ice Surface Classification codes: DOI: 10.5281/zenodo.2598122

Spectra Processing codes: DOI: 10.5281/zenodo.2598219

Field and associated data: 10.5281/zenodo.2598479

The active repositories for ongoing development of BioSNICAR_GO and the ice surface classifiers codes are at www.github.com/jmcook1186/BioSNICAR_GO and www.github.com/jmcook1186/IceSurfClassifiers respectively.

Codes and datasets used in this study are available at our data repository. For initial submission we provide the temporary repository <https://drive.google.com/open?id=1AgWhHoGPnYXPVf9PGLIDkuTRVF7qYkQ> to enable updates based on reviewer comments. For final publication we will mint a digital object identifier at a formal repository. The active repositories for ongoing development of BioSNICAR_GO and the ice surface classifiers codes are at www.github.com/jmcook1186/BioSNICAR_GO and www.github.com/jmcook1186/IceSurfClassifiers respectively.

6 Author Contribution Statement

JC developed the measurement protocol, gathered field measurements, analysed the data, wrote the main codes, curated the data repository, produced the figures and wrote the manuscript. OMcA was instrumental in building and testing the UAV. AT, CW, JMcC, SH, TG gathered crucial field data. CW provided essential advice regarding microscopy and biological sampling protocols and helped with experimental design, and also led the empirical measurements of glacier algae pigmentation and absorption coefficients. AT wrote the code for radiometric calibration of multispectral imagery from the UAV and post-processed the UAV images. AT also derived 2016 and 2017 dark-ice extent from MODIS imagery, analysed MAR snow depth outputs and produced Fig 6, translated the energy balance model into python⁴ and made significant contributions to the manuscript writing and experimental design. JMcC and SM provided cleaned mineral dust and particle size distribution data to feed into the radiative transfer model and JMcC provided useful discussions regarding experimental design. MS provided DISORT modelling and estimates of mineral dust refractive indices. MF helped develop the bio-optical model. RB provided expert advice regarding field spectroscopy and helped measure mineral dust refractive indices in the laboratory. AJH helped develop the experimental design. AH, JR and AMcG both provided expert advice on UAV remote-sensing. JR, DvA and AH modelled runoff from the GrIS dark zone. AD provided microscopy images from field samples. Other authors commented on the style and content of the final manuscript.

7 Acknowledgements

JC, AT, AJH, CW, AD, SH, AmcG, AA, TDLIF, EH, MY, TG and MT acknowledge funding from UK National Environmental Research Council Large Grant NE/M021025/1 ‘Black and Bloom’. JC gratefully acknowledges the Rolex Awards for Enterprise, National Geographic and Microsoft (“AI for Earth”). LGB, JMcC and JBM acknowledge funding from the UK National Environmental Research Council Large Grant NE/M020770/1 ‘Black and Bloom’ and LGB and SM acknowledge funding from the German Helmholtz Recruiting Initiative (award number I-044-16-01). JC gratefully acknowledges the Rolex Awards for Enterprise, National Geographic and Microsoft (“AI for Earth”). TG acknowledges the Gino Watkins Memorial Fund and Nottingham Education Trust. Greenland Analogue Project (GAP) weather station data are made available through the Programme for Monitoring of the Greenland Ice Sheet (www.promice.dk). MAR v3.8.1 regional climate model outputs used estimate mean snow depth were provided by Xavier Fettweis.

References

- 1030 | [Aoki, T., Kuchiki, K., Niwano, M., Matoba, S., Uetake, J., Masuda, K., Ishimoto, H. Numerical simulation of spectral albedos of glacier surfaces covered with glacial microbes in Northwestern Greenland. AIP Conference Proceedings, 1531, 176, doi: 10.1063/1.4804735, 2013.](#)
- | **Bamber, J., Westaway, R.M., Marzeion, B., Wouters, B.:** (2018): **The land ice contribution to sea level during the satellite era. Environmental Research Letters, 13 063008**~~online 8th May 2018~~, doi: [10.1088/1748-9326/aac2f0](#), 2018.
- 1035 | **Benning, L. G., Anesio, A. M., Lutz, S., & Tranter, M.**-(2014)-: **Biological impact on Greenland’s albedo. Nature Geoscience, 7** (10), 691. doi: [20.1038/ngeo2260](#), 2014.
- | [Blankenship, R.E., Tiede, D.M., Barber, J., Brudvig, G.W., Fleming, G., Ghirardi, M., Gunner, M.R., Junge, W., Kramer, D.M., Melis, A., Moore, T.A., Moser, C.C., Nocera, D.G., Nozik, A.J., Ort, D.R., Parson, W.W., Prince, R.C., Sayre, R.T.](#)
- 1040 | [: Comparing photosynthetic and photovoltaic efficiencies and recognizing the potential for improvement. Science, 332: 805–809, 2011.](#)
- |
- |
- 1045 |
- | **Bøggild, C.E., Brandt, R.E., Brown, K.J., Warren, S.G.**-(2010)**G.:** **The ablation zone in northeast Greenland: ice types, albedos and impurities. Journal of Glaciology, 56 (195): 101-113, 2010.**
- |
- 1050 | **Box, J. E., Fettweis, X., Stroeve, J. C., Tedesco, M., Hall, D. K., and Steffen, K.**-(2012): **Greenland ice sheet albedo feedback: thermodynamics and atmospheric drivers, The Cryosphere, 6, 821–839, doi:10.5194/tc-6-821-2012, 2012.**
- | [Brock, B. W., Arnold, N.S.: A spreadsheet-based \(Microsoft Excel\) point surface energy balance model for glacier and snow melt studies. Earth Surface Processes and Landforms, 25\(6\), 649–658. doi:10.1002/1096-9837\(200006\)25:6<649::aid-esp97>3.0.co;2-u, 2012.](#)
- 1055 |
- | [Cook, J.M., Edwards, A., Irvine-Fynn, T.D.I., Takeuchi, N. Cryoconite: Dark biological secret of the cryosphere, Progress in Physical Geography, 40: 66 – 111, https://doi.org/10.1177/0309133315616574, 2015a.](#)

1060 | [Cook, J.M., Edwards, A., Hubbard, A.: Biocryomorphology: Integrating Microbial Processes with Ice Surface Hydrology, Topography, and Roughness, *Frontiers in Earth Science*, 3 \(78\), doi: 10.3389/feart.2015.00078, 2015b.](#)

1065 | [Cook, J. M., Hodson, A. J., Taggart, A. J., Mernild, S. H., and Tranter, M.-\(2017a\).: A predictive model for the spectral “bioalbedo” of snow, *J. Geophys. Res.-Earth Surf.*, 122, 434–454, <https://doi.org/10.1002/2016JF003932>., 2017a.](#)

1070 | [Cook JM, Hodson AJ, Gardner AS, Flanner M, Tedstone AJ, Williamson C, Irvine-Fynn TD, Nilsson J, Bryant R, Tranter M. 2017: Quantifying bioalbedo: A new physically-based model and critique of empirical methods for characterizing biological influence on ice and snow albedo. *The Cryosphere Discussions*: 1–29. DOI: 10.5194/tc-2017-73, 2017b](#)

1075 | [Dauchet, J., Blanco S., Cornet, J-F., Fournier, R: Calculation of radiative properties of photnthetic microorganisms. *Journal of Quantitative Spectroscopy and Radiative Transfer*, 161: 60-84, 2015.](#)

1080 | [Dee, D.P., Uppala, S.M., Simmons, A.J., Berrisford, P., Poli, P., Kobayashi, S., Andrae, U., Balmaseda, M.A., Balsamo, G., Bauer, P., Bechtold, P., Beljaars, A.C.M., van de Berg, L., Bidlot, J., Bormann, N., Delsol, C., Dragani, R., Fuentes, M., Geer, A.J., Haimberger, L., Healy, S.B., Hersbach, H., Holm, E.V., Isaksen, L., Kallberg, P., Kohler, M., Matricardi, M., McNally, A.P., Monge-Sanz, B.M., Morcrette, J-J., Park, B-K., Peubey, C., de Rosnay, P., Tavolato, C., Thepaut, J-N., Vitart, F.-\(2011\): The ERA-Interim reanalysis: configuration and performance of the data assimilation system. *Quarterly Journal of the Royal Meteorological Society*, 137 \(656\): 553-597, doi: 10.1002/qj.828, 2011.](#)

1085 | [Dial, R., Ganey, G., Skiles, S.M.-\(2018\): What colour should glacier algae be? An ecological role for red carbon in the cryosphere. *FEMS Microbiology Ecology*, 94 \(3\): fiy2007, doi: 10.1093/femsec/fiy007, 2018.](#)

1090 | [Enderlin, E. M., Howat, I. M., Jeong, S., Noh, M.-J., van Angelen, J. H., van den Broeke, M. R.-\(2014\): An improved mass budget for the Greenland ice sheet, *Geophysical Research Letters*, 41, 866–872, doi:10.1002/2013GL059010, 2014.](#)

1090 | [Fettweis, X., Box, J. E., Agosta, C., Amory, C., Kittel, C.,-and Gallée, H-\(2016\): Reconstructions of the 1900–2015 Greenland ice sheet surface mass balance using the regional climate MAR model, *The Cryosphere Discussions*, 2016, 1–32, doi:10.5194/tc-2016-268, 2016.](#)

- Flanner, M. G., Zender, C. S., Randerson, J. T., and Rasch, P. J.-(2007): Present-day climate forcing and response from black carbon in snow, *J. Geophys. Res.*, 112, D11202, <https://doi.org/10.1029/2006JD008003>, 2007.
- 1095 Ganey, G.Q., Loso, M.G., Burgess, A.B., Dial, R.J.-(2017): The role of microbes in snowmelt and radiative forcing on an Alaskan icefield. *Nature Geoscience*, 10, 754–759. <https://doi.org/10.1038/ngeo3027>, 2017.
- Green, R. O., Dozier, J., Roberts, D., and Painter, T. H.-(2002): Spectral snow-reflectance models for grain size and liquid water fraction in melting snow for the solar reflected spectrum, *An. Glaciol.*, 34, 71–73, 2002.
- 1100 Haardt, H. and Maske, H.-(1987): Specific in vivo absorption coefficient of chlorophyll a at 675 nm, *Limnol. Oceanogr.*, 32, 608–619, 1987.
- 1105 Hanna, E., Navarro, F.J., Pattyn, F., Domingues, C.M., Fettweis, X., Ivins, E.R., Nicholls, R.J., Ritz, C., Smith, B., Tulaczyk, S., Whitehouse, P., Zwally, J.-(2013): Ice sheet mass balance and climate change. *Nature*, 498 (7452): 51 – 59, doi: 10.1038/nature12238, 2013.
- Hillebrand H, Dürselen C-D, Kirschtel D.-et al-(1999), Pollinger, U., Zohary, T: Biovolume calculation for pelagic and benthic microalgae. *J Phycol* 1999;35:403–24, 1999.
- 1110 Howat, I. M., Negrete, A. & Smith, B. E.: The Greenland Ice Mapping Project (GIMP) land classification and surface elevation data sets. *The Cryosphere*, 8, 1509–1518, (2014).
- 1115 Kirk, J.T.O.-(1976): A theoretical analysis of the contribution of algal cells to the attenuation of light within natural waters III. Cylindrical and spheroidal cells. *New Phytologist*, 77: 341-358, 1976.
- Knap, W.H.; Brock, B.W.; Oerlemans, J.; Willis, I.C.: Comparison of Landsat TM- derived and ground-based albedos of Haut Glacier d’Arolla, Switzerland. *Int. J. Remote Sens.* 1999, 20, 3293–3310, 1999.
- 1120 Langen, P.L., Fauso, R.S., Vendecrux, B., Mottram, R.H., Box, J.E-(2017): Liquid water flow and retention on the Greenland Ice Sheet in the regional climate model HIRHAM5: local and large scale impacts. *Frontiers in Earth Science*, 4 (110), doi: 10.3389/feart.2016.00110, 2017.
- 1125 Lee, E., Pilon, L.: Absorption and scattering by long and randomly oriented linear chains of spheres. *Journal of the Optical Society of America*, 30 (9): 1892- 1900, 2013.

- Liang, S., 2001: Narrowband to broadband conversions of land surface albedo I. *Remote Sens. Environ.* 76, 213–238. [https://doi.org/10.1016/S0034-4257\(00\)00205-4](https://doi.org/10.1016/S0034-4257(00)00205-4), 2001.
- 1130 Lutz, S., McCutcheon, J., McQuaid, J.B., Benning, L.G. (2018): The diversity of ice algal communities on the Greenland Ice Sheet revealed by oligotyping. *Microbial Genomics*, 4: 1-10, doi: 10.1099/mgen.0.000159, 2018.
- Masojídek, J., Torzillo, G., Koblížek, M.: Photosynthesis in Microalgae. In *Handbook of Microalgal Culture* (eds A. Richmond and Q. Hu). doi:10.1002/9781118567166.ch2, 2013
- 1135 Morel, A. and Bricaud, A.: Theoretical results concerning light absorption in a discrete medium, and application to specific absorption of phytoplankton, *Deep-Sea Res.*, 28, 1375–1393, 1981
- Muller, F., Keeler, C.M.: Errors in short term ablation measurements on melting ice surfaces. *Journal of Glaciology*, 8 (52): 91-105, 1969.
- 1140
- Ngheim, S.V., Hall, D.K., Mote, T.L., Tedesco, M. Albert, M.R., Keegan, K., Shuman, C.A., DiGirolamo, N.E., Neumann, G. (2012): The extreme melt across the Greenland Ice Sheet in 2012. *Geophysical Research Letters*, 39, L20502, doi: 10.1029/2012GL053611, 2012.
- 1145
- Noel, B., van de Berg, W.J., Machguth, H., Lhermitte, S., Howat, I., Fettweis X., Van den Broecke, M.R. (2016): A daily, 1km resolution data set of downscaled Greenland Ice Sheet surface mass balance (1958-2015). *The Cryosphere*, 10: 2361-2377, doi: 10.5194/tc-10-2361-2016, 2016.
- 1150
- Nolin, A.W., Dozier, J. (2000): A hyperspectral method for remotely sensing the grain size of snow. *Remote Sensing of Environment*, 74: 207-216, 2000.
- Nordenskiöld, A. E.: Cryoconite found 1870, 19–25 July, on the inland ice, east of Auleitsivik Fjord, Disco Bay, Greenland. *Geol. Mag.*, 2, 157–162, 1875.
- 1155
- Painter, T. H., Duval, B., and Thomas, W. H. (2001): Detection and quantification of snow algae with an airborne imaging spectrometer, *Appl. Environ. Microbiol.*, 67, 5267–5272, <https://doi.org/10.1128/AEM.67.11.5267-5272.2001>, 2001.

- 1160 Remias, D., Schwaiger, S., Aigner, S., Leya, T., Stuppner, H., Lutz, C.-(2012): Characterization of an UV- and VIS-absorbing, purpurogallin-derived secondary pigment new to algae and highly abundant in *Mesotaenium berggrenii* (Zygnematophyceae, Chlorophyta), an extremophyte living on glaciers, *FEMS Microbiol. Ecol.*, 79, 638–648, <https://doi.org/10.1111/j.1574-6941.2011.01245.x>, 2012.
- 1165 Rueden, C.T., Schindelin, J., Hiner, M.C., DeZonia, B.E., Walter, A.E., Arena, E.T., Eliceiri, K.W.-(2017): ImageJ2: ImageJ for the next generation of scientific image data. *BMC Bioinformatics*, 18: 529 doi: 10.1186/s12859-017-1934-z, 2017
- 1170 Ryan, J., Hubbard, A., Irvine-Fynn, T.D., Doyle, S.H., Cook, J.M., Stibal, M., Box, J.E.,-2017;: How robust are in situ observations for validating satellite-derived albedo over the dark zone of the Greenland Ice Sheet? *Geophysical Research Letters*, 44 (12): 6218 – 6225, 2017.
- 1175 Ryan, J., Hubbard, A., Irvine-Fynn, Cook, J., T., Smith, L.C., Cameron, K., Box, J.E.-(2018a): Dark zone of the Greenland Ice Sheet controlled by distributed biologically-active impurities. *Nature Communications*, 9, 1065: doi: 10.1038/s41467-018-03353-2, 2018a.
- 1180 Ryan, J., van As, D., Cooley, S.W., Cooper, M.G., Pitcher, L.H., Hubbard, A.-(2018): Greenland Ice Sheet surface melt amplified by snow_line migration and bare ice exposure. *Science Advances*, 5 (3): eeav3738, doi: 10.1126/sciadv.aav3738, 2018b.
- Sanna, L., Romeo, A. Mineralogy and geochemistry of cryoconite sediments in Ekip Sermia glacier (central-west Greenland). *Journal of Mediterranean Earth Sciences*, 10: 159-166, 2018.
- 1185 Seager, S., Turner, E.-L., Schafer, J.,-and Ford, E.-B.-(2005): Vegetation's red edge: a possible spectroscopic biosignature of extraterrestrial plants, *Astrobiology*, 5, 372–390, 2005.
- 1190 Shepherd, A., Ivins, E. R., A-G.,-Barletta, V. R., Bentley, M. J., Bettadpur, S., Briggs, K. H., Bromwich, D. H., Forsberg, R., Galin, N., Horwath, M., Jacobs, S., Joughin, I., King, M. A., Lenaerts, J. T. M., Li, J., Ligtenberg, S. R. M., Luckman, A., Luthcke, S. B., McMillan, M., Meister, R., Milne, G., Mouginot, J., Muir, A., Nicolas, J. P., Paden, J., Payne, A. J., Pritchard, H., Rignot, E., Rott, H., Sohn, H.-G.,-Rensen, L. S., Scambos, T. A., Scheuchl, B., Schrama, E. J. O., Smith, B., Sundal, A. V., van Angelen, J. H., van de Berg, W. J., van den Broeke, M. R., Vaughan, D. G.,

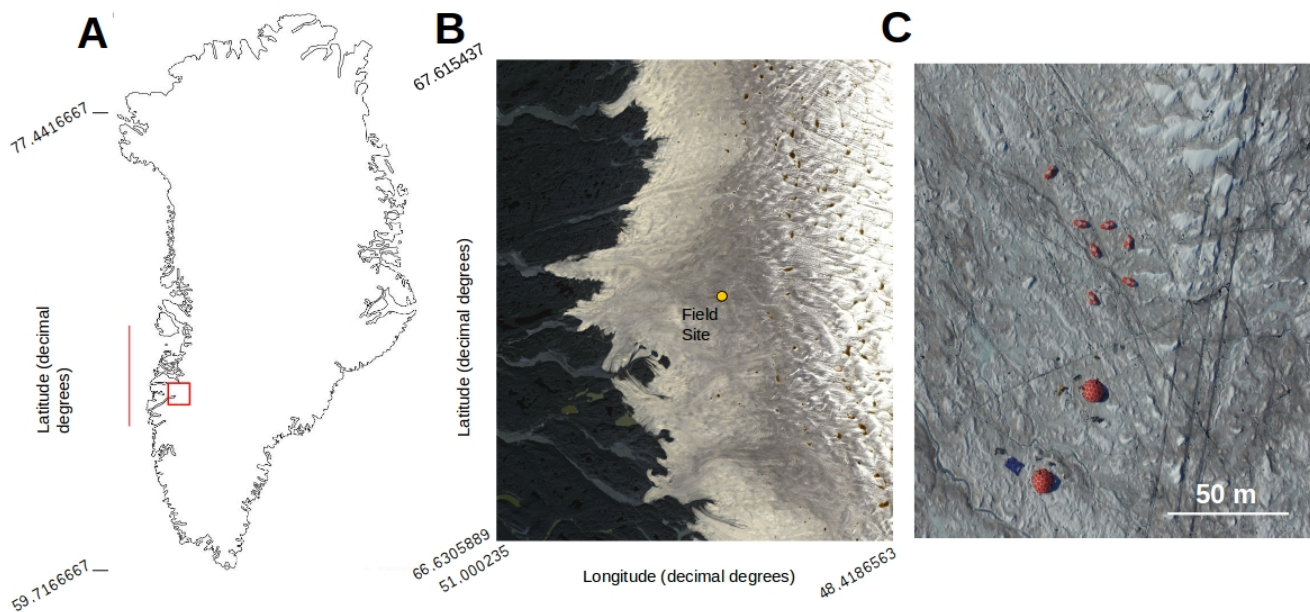
- Velicogna, I., Wahr, J., Whitehouse, P. L., Wingham, D. J., Yi, D., Young, D., and Zwally, H. J. (2012): A Reconciled Estimate of Ice-Sheet Mass Balance, *Science*, 338, 1183–1189, doi:10.1126/science.1228102, 2012.
- 1195 Shimada, R., Takeuchi, N., and Aoki, T.: Inter-annual and geographical variations in the extent of bare ice and dark ice on the Greenland ice sheet derived from MODIS satellite images, *Frontiers in Earth Science*, 4, doi:10.3389/feart.2016.00043
- 1200 Skiles, S. M., Painter, T. H., and Okin, G. S.: (2017)–A method to retrieve the spectral complex refractive index and single scattering optical properties of dust deposited in mountain snow, *J. Glaciol.*, 63, 133–147, <https://doi.org/10.1017/jog.2016.126>, 2017.
- 1205 Smeets, C. J. P. P., Van den Broeke, M. R.: Temporal and spatial variations of the aerodynamic roughness length in the ablation zone of the Greenland ice sheet, *Bound.-Lay. Meteorol.*, 128, 315–338, <https://doi.org/10.1007/s10546-008-9291-0>, 2008.
- 1210 Smith, L.C., Yang, K., Pitcher, L.H., Overstreet, B.T., Chu, V.W., Rennermalm, A., Ryan, J.C., Cooper, M.G., Gleason, C.J., Tedesco, M., Jeyaratnam, J., van As, D., van den Broeke, M.R., van de Berg, W.J., Noel, B., Langen, P.L., Cullather, R.I., Zhao, B., Willis, M.J., Hubbard, A., Box, J.E., Jenner, B.A., Behar, A.E. (2017): Direct measurements of meltwater runoff on the Greenland ice sheet surface. *PNAS*, 114 (50): E10622 – E10631, <https://doi.org/10.1073/pnas.1707743114>, 2017.
- 1215 Stibal, M., Box, J.E., Cameron, K.A., Langen, P.L., Yallop, M., Mottram, R.H., Khan, A.L., Molotch, N.P., Christmas, N.A.M., Quaglia, F.C., Remias, D., Smeets, C.J.P., van den Broeke, M.R., Ryan, J.C., Hubbard, A., Tranter, M., van As, D., Ahlstrøm, A.P. (2017): Algae drive enhanced darkening of bare ice on the Greenland Ice Sheet. *Geophysical Research Letters*, 44 (11): 11463–11471, 2017.
- 1220 Stroeve, J., Box, J. E., Wang, Z., Schaaf, C., and Barrett, A. (2013): Re-evaluation of MODIS MCD43 Greenland albedo accuracy and trends. *Remote Sensing of Environment*, 138, 99–214. doi: 10.1016/j.rse.2013.07.023, 2013.
- Tedesco, M., Foreman, C., Anton, J., Steiner, N., Schwartzman, T.: Comparative analysis of morphological, mineralogical and spectral properties of cryoconite in Jakobshavn Isbræ, Greenland, and Canada Glacier, Antarctica. *Annals of Glaciology*, 54(63), 147–157. doi:10.3189/2013AoG63A417, 2013.
- 1225 Uetake, J., Naganuma, T., Hebsgaard, M. B., Kanda, H., and Kohshima, S. (2010) Communities of algae and cyanobacteria on glaciers in west Greenland, *Polar Science*, 4, 71–80, doi:<http://dx.doi.org/10.1016/j.polar.2010.03.002>

- 1230 Tedesco, M., Doherty, S., Fettweis, X., Alexander, P., Jeyaratnam, J., Nobel, E., Stroeve, J.: The darkening of the Greenland ice sheet trends, drivers and projections (1981 – 2100), *The Cryosphere*, 10, 477-496, doi: 10.5194/tc-10-477-2016, 2016.
- 1235 Tedstone, A.J., Bamber, J.L., Cook, J.M., Williamson, C.J., Fettweis, X., Hodson, A.J., Tranter, M., 2017: Dark ice dynamics of the south-west Greenland Ice Sheet, *The Cryosphere Discuss*, doi: <https://www.the-cryosphere-discuss.net/tc-2017-79/>, 2017
- Toon, O. B., McKay, C. P., Ackerman, T. P., Santhanam, K.: Rapid calculation of radiative heating rates and photodissociation rates in inhomogeneous multiple scattering atmospheres, *J. Geophys. Res.*, 94(D13), 16287– 16301, doi:10.1029/JD094iD13p16287, 1989.
- 1245 Uetake, J., Naganuma, T., Hebsgaard, M. B., Kanda, H., and Kohshima, S.: Communities of algae and cyanobacteria on glaciers in west Greenland, *Polar Science*, 4, 71 – 80, doi: <http://dx.doi.org/10.1016/j.polar.2010.03.002>, 2010.
- Van As, D., Van den Broeke, M. R., Reijmer, C. H., and Vande Wal, R. S. W.: The summer surface energy balance of the high Antarctic Plateau, *Bound. Lay. Meteorol.*, 115, 289–317, <https://doi.org/10.1007/s10546-004-4631-1>, 2005.
- 1250 van As, D., Hubbard, A. L., Hasholt, B., Mikkelsen, A. B., van den Broeke, M. R., and Fausto, R. S.: Large surface meltwater discharge from the Kangerlussuaq sector of the Greenland ice sheet during the record-warm year 2010 explained by detailed energy balance observations, *The Cryosphere*, 6, 199-209, <https://doi.org/10.5194/tc-6-199-2012>, 2012.
- 1255 van As, D., Bech Mikkelsen, A., Holtegaard Nielsen, M., Box, J. E., Claesson Liljedahl, L., Lindbäck, K., Pitcher, L., and Hasholt, B.: Hypsometric amplification and routing moderation of Greenland ice sheet meltwater release, *The Cryosphere*, 11, 1371-1386, <https://doi.org/10.5194/tc-11-1371-2017>, 2017.
- 1260 van den Broeke, M. R., Enderlin, E. M., Howat, I. M., Kuipers Munneke, P., Noël, B. P. Y., van de Berg, W. J., van Meijgaard, E., and Wouters, B. (2016): On the recent contribution of the Greenland ice sheet to sea level change, *The Cryosphere*, 10, 1933–1946, doi:10.5194/tc-10-1933-2016, 2016.

- 1265 | **van Diedenhoven, B., Ackerman, A.S., Cairns, B., Fridlind, A.M.-(2014): A flexible parameterization for shortwave optical properties of ice crystals. *Journal of the Atmospheric Sciences*, 71: 1763 – 1782, doi:10.1175/JAS-D-13-0205.1, 2014.**
- 1270 | **Warren, S. G.: (1982)-Optical properties of snow, *Rev. Geophys.*, 20, 67–89, <https://doi.org/10.1029/RG020i001p00067>, 1982.**
Warren, S. G., Brandt, R. E.: Optical constants of ice from the ultraviolet to the microwave: A revised compilation, *J. Geophys. Res.*, 113, D14220, <https://doi.org/10.1029/2007JD009744>, 2008, 2008.
Warren, S. G. and, Wiscombe, W. J.-(1980): A model for the spectral albedo of snow. 11. Snow containing atmospheric aerosols, *J. Atmos. Sci.*, 37, 2734–2745, 1980.
- 1275 | **Wharton, R.A., McKay, C.P., Simmons, G.M., Parker, B.C.: Cryoconite holes on glaciers. *BioScience*, 35 (8): 499-503, 1985.**
- 1280 | **Wientjes, I. G. M., Oerlemans, J.-(2010): An explanation for the dark region in the western melt zone of the Greenland ice sheet, *The Cryosphere*, 4, 261–268, <https://doi.org/10.5194/tc-4-261-2010>, 2010.**
Wientjes, I.G.M., Van de Wal, R.S.W., Reichert, G.J., Sluijs, A., Oerlemans, J.-(2011): Dust from the dark region in the western ablation zone of the Greenland Ice Sheet. *The Cryosphere*, 5, 589–601, 2011, doi:10.5194/tc-5-589-2011, 2011.
- 1285 | **Williamson, C.J., Anesio, A.M., Cook, J., Tedstone, A., Poniecka, E., Holland, A., Fagan, D., Tranter, M., Yallop, M.L. 2018: Ice algal bloom development on the surface of the Greenland Ice Sheet, *FEMS Microbiology Ecology*, fty025, <https://doi.org/10.1093/femsec/fty025>, 2018.**
Williamson, C.J., Cameron, K.A., Cook, J.M., Zarsky, J.D., Stibal, M., Edwards, A.: Glacier Algae: A Dark Past and a Darker Future. *Front. Microbiol.* 10:524. doi: 10.3389/fmicb.2019.00524, 2019.
- 1290 | **Yallop, M. L., Anesio, A. J., Perkins, R. G., Cook, J., Telling, J., Fagan, D., MacFarlane, J., Stibal, M., Barker, G., Bellas, C., Hodson, A., Tranter, M., Wadham, J., and Roberts, N. W.-(2012): Photophysiology and albedo-changing potential of the ice-algal community on the surface of the Greenland ice sheet, *ISME J.*, 6, 2302–2313, 2012.**

1295

1300



1305

1310

1315

Fig 1: A) Map of Greenland showing the bounding box of the Sentinel-2 tile containing our field site (red box) and the latitudinal extent of our runoff modelling (red line). The area in the red box is presented in detail in B) with our field site marked with a yellow dot.

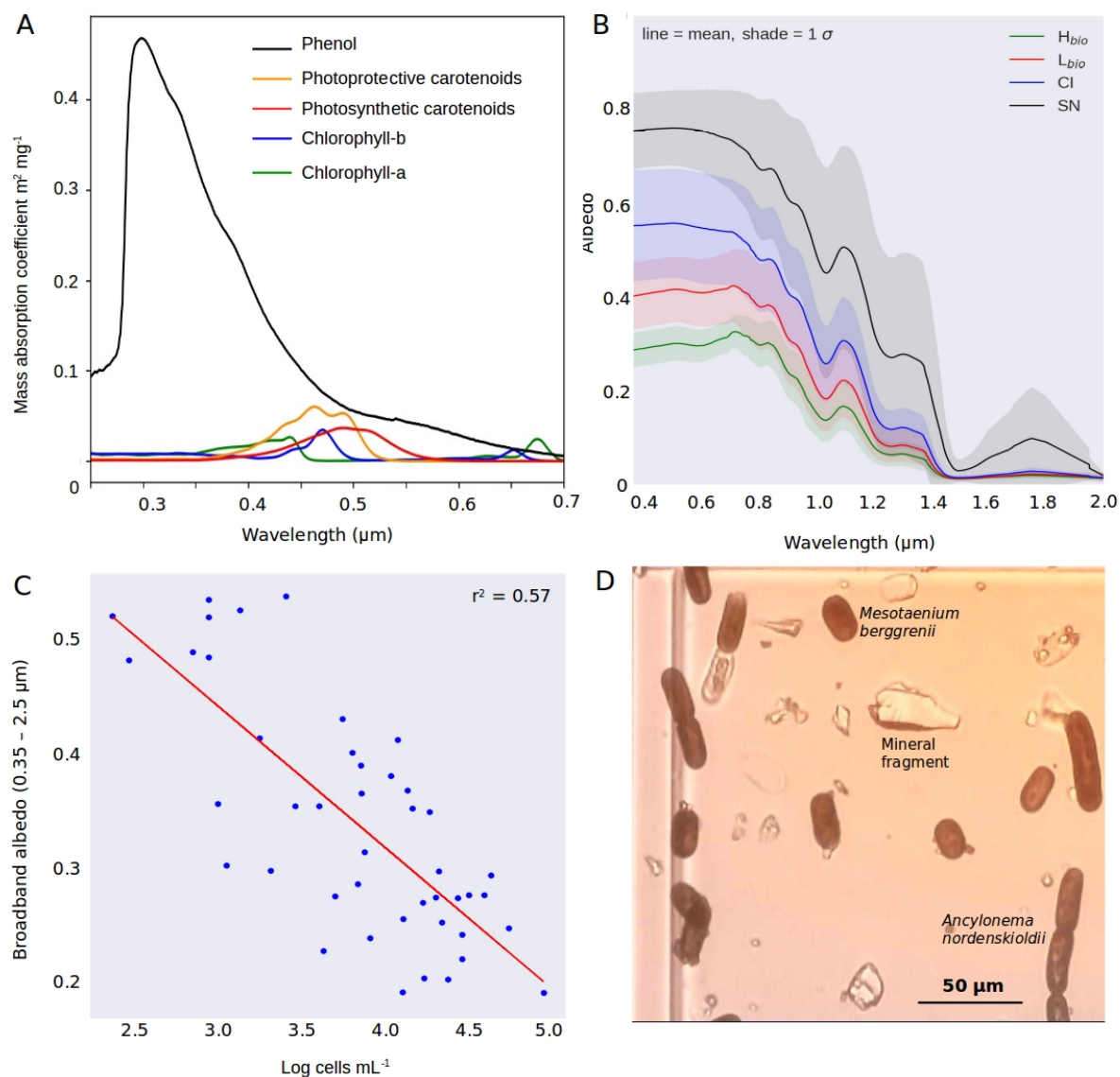


Fig 2 A) Aerial image of our field camp in the Greenland Dark Zone; B) Microscope image of melted Hbio ice sample, showing the two dominant algal species; C) Measured spectral albedos for each surface type, D) plot showing the natural logarithm of cell abundance against broadband albedo

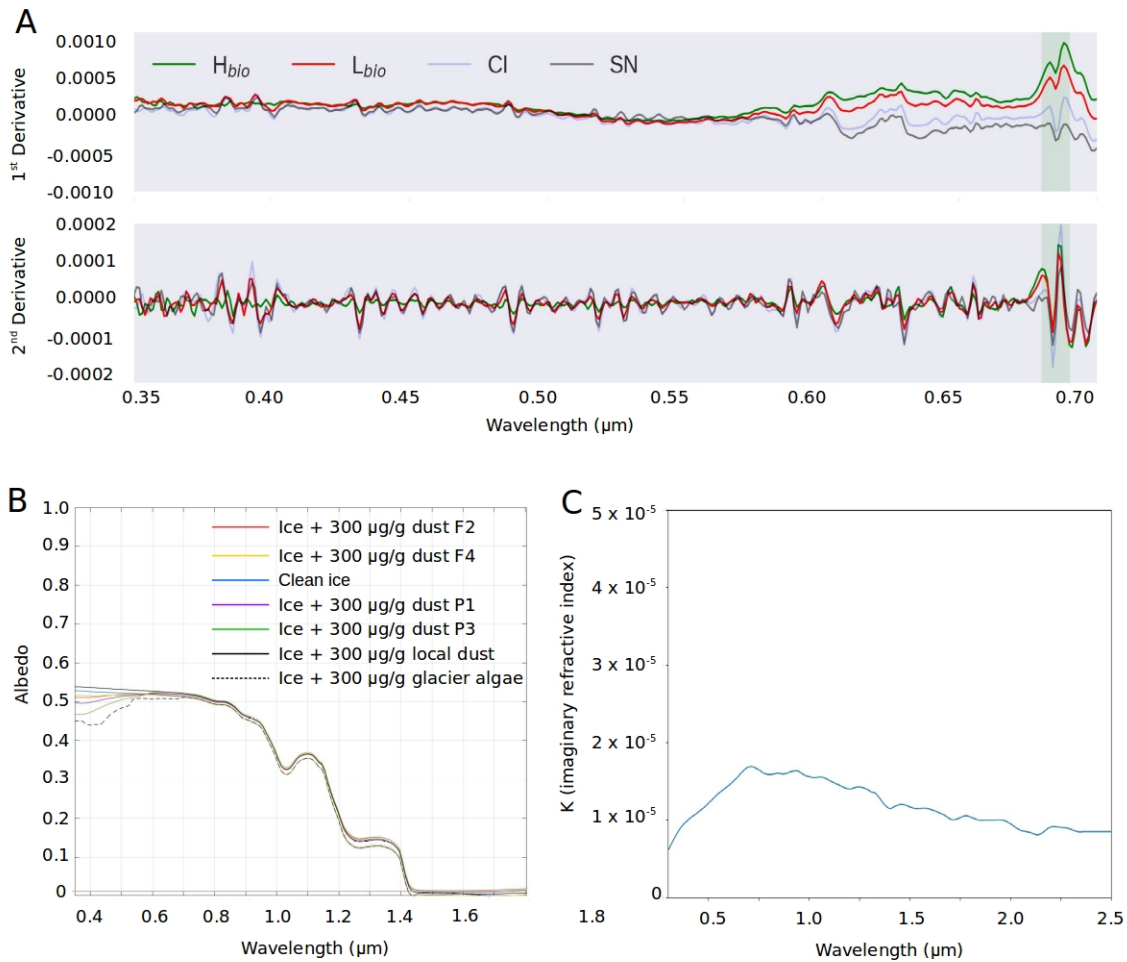
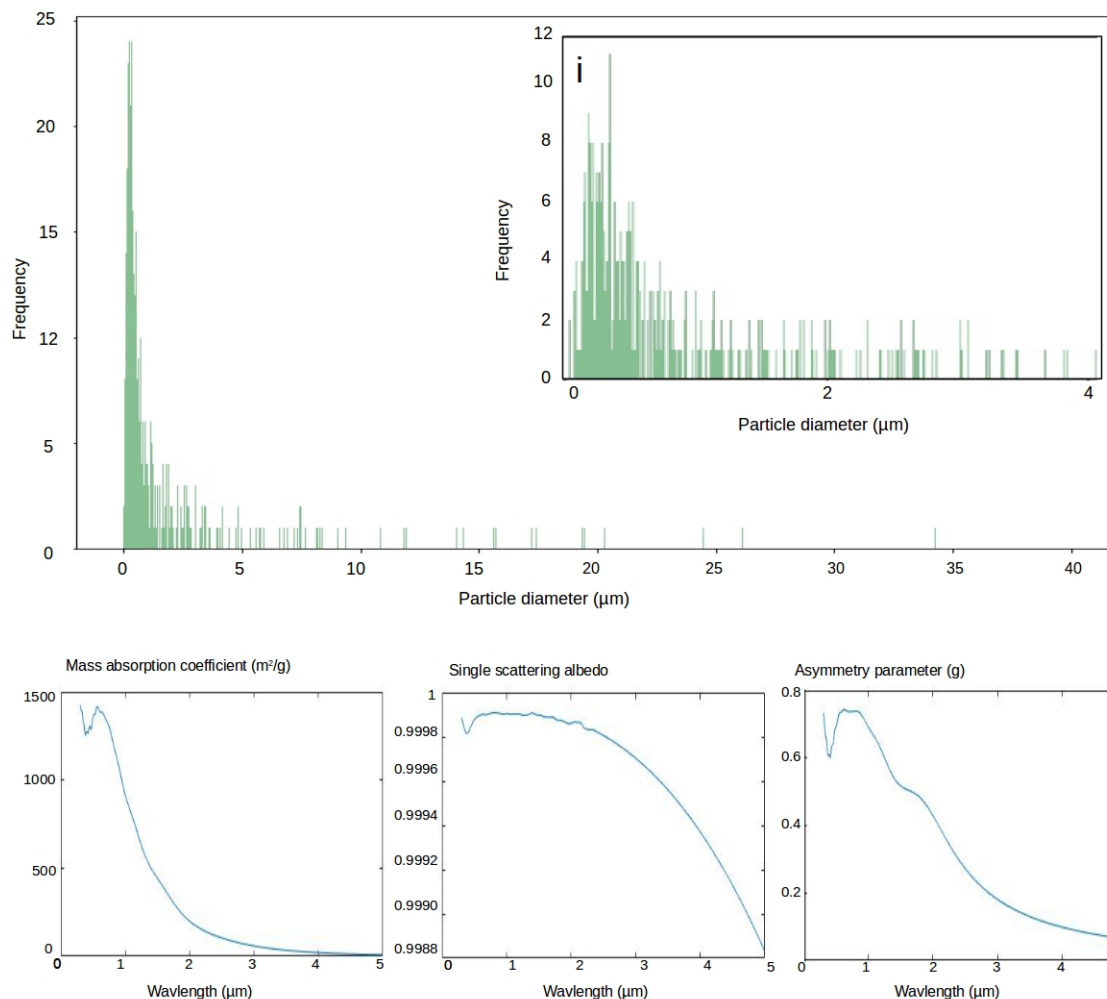


Figure 32: A) First and second derivative spectra for each surface class; B) Imaginary refractive index for the local mineral dust; C) BioSNICAR_GO modelled spectral albedo for clean ice (blue), ice with 300 $\mu\text{g/g}$ mineral dust in the upper 3 mm (red for Polashenski et al. 2015 low hematite dust, yellow for Polashenski et al. 2015 medium hematite dust) and ice with 300 $\mu\text{g/g}$ algae in the upper 3 mm (yellowpurple).



scattering albedo calculated using Lorenz-Mie theory for the mineral dust sample, D) asymmetry parameter calculated using Lorenz-Mie theory for the mineral dust sample.

Fig 35: A) Classified map of the area shown in C for 2016. B) ABroadband albedo map of the area shown in C for 2016. C) RGB “true colour” image showing the Sentinel 2 tile covering our field site in the Kangerlussuaq area. D) Classified map of the area shown in C for 2017. E) Broadband Albedo map of the area shown in C for 2017. F) Classified map of a 200 x 200 m area at the field site marked in C imaged using a UAV mounted multispectral camera. G) ABroadband albedo map of a 200 x 200 m area at the field site marked in C imaged using a UAV mounted multispectral camera. Panels A, B, C, D, E all use UTM Zone 22 projection and have pixel resolution of 20 m. All Sentinel 2 data was preprocessed from L1C to L2A using Sen2Cor and non-ice areas masked using the MeASURES GIMP mask. Classified and albedo maps for additional Sentinel 2 tiles are shown in Supplementary Information 4.

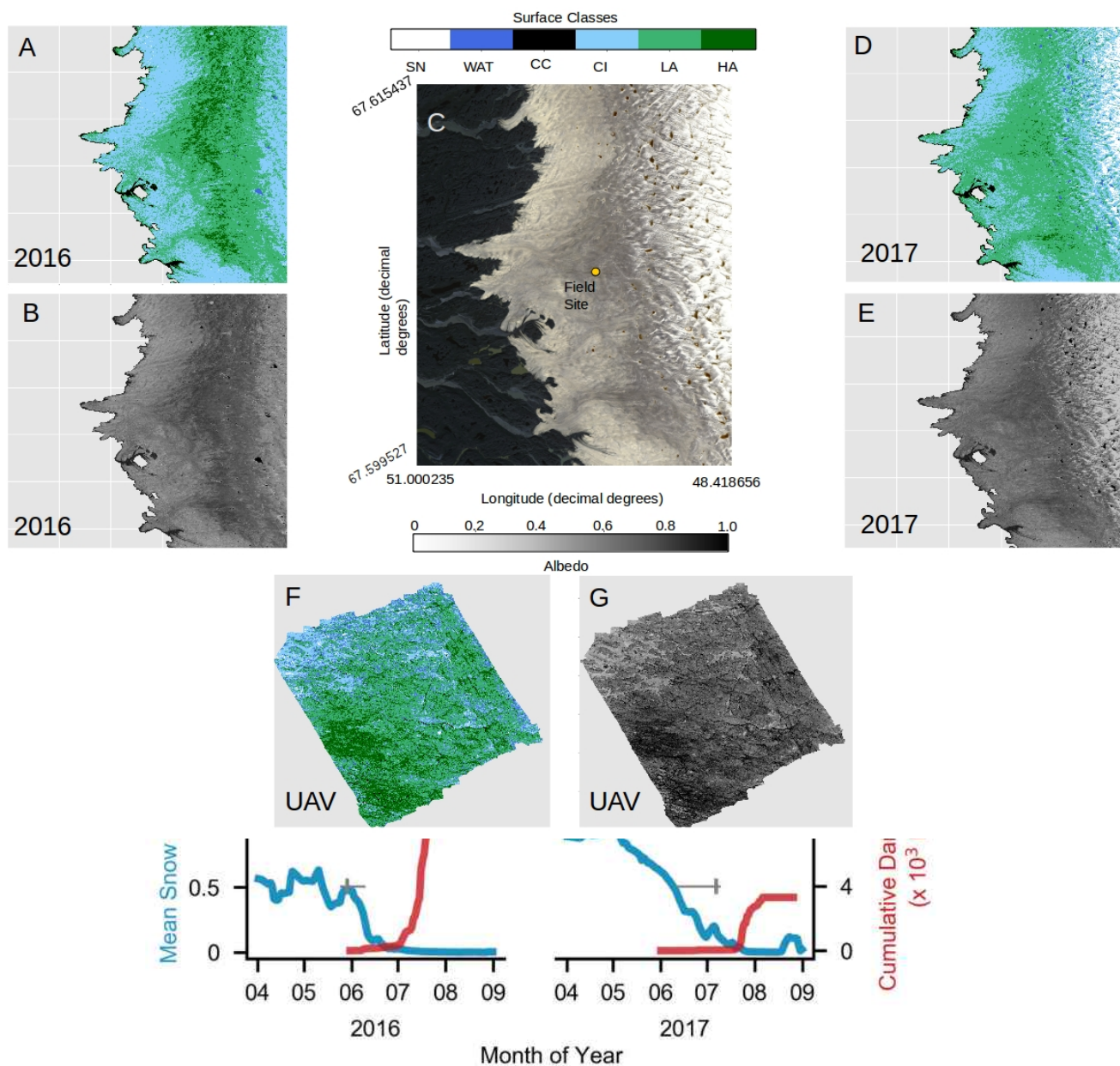


Figure 46: (A,B) Dark-ice duration on the south-west GrIS in summers 2016 and 2017, expressed as a percentage of the total daily cloud-free observations made during June-July-August (JJA). Each year is labelled with dark-ice extent. In each year, pixels that are dark for fewer than 5 days are not shown. (C,D) Average snow depth modelled by MAR (blue) and cumulative dark-ice extent observed by MODIS (red) (Tedstone et al., 2017) during April to August. Vertical bars (grey) denote median date of snow clearing derived from MODIS; horizontal bars denote the interquartile range of the day of year of bare-ice appearance.

1370

<u>100 ug/g</u>	<u>Local dust</u>	<u>P1</u>	<u>P2</u>	<u>P3</u>	<u>F1</u>	<u>F2</u>	<u>F3</u>	<u>F4</u>	<u>Glacier algae</u>
<u>Albedo change</u>	<u>+0.0025</u>	<u>-0.0007.38</u>	<u>-0.0016</u>	<u>-0.0039</u>	<u>+0.0032</u>	<u>+0.000167</u>	<u>-0.0012</u>	<u>-0.0013</u>	<u>-0.0065</u>

<u>300 ug/g</u>	<u>Local dust</u>	<u>P1</u>	<u>P2</u>	<u>P3</u>	<u>F1</u>	<u>F2</u>	<u>F3</u>	<u>F4</u>	<u>Glacier algae</u>
<u>Albedo change</u>	<u>+0.0084</u>	<u>-0.00054</u>	<u>-0.0029</u>	<u>-0.0092</u>	<u>+0.011</u>	<u>+0.0024</u>	<u>-0.0024</u>	<u>-0.0033</u>	<u>-0.019</u>

<u>500 ug/g</u>	<u>Local dust</u>	<u>P1</u>	<u>P2</u>	<u>P3</u>	<u>F1</u>	<u>F2</u>	<u>F3</u>	<u>F4</u>	<u>Glacier algae</u>
<u>Albedo change</u>	<u>+0.0145</u>	<u>+0.000096</u>	<u>-0.0033</u>	<u>-0.0128</u>	<u>+0.0185</u>	<u>+0.0049</u>	<u>-0.0031</u>	<u>-0.0052</u>	<u>-0.029</u>

1375 | Table 1: Albedo change relative to clean ice resulting from the addition of 100, 300 and 500 ug/g of each mineral dust.

A:			
Surface Type	Mean	Standard Ødeviation	Number of observations
WAT	0.31	0.017	154070
CC	0.09	0.031	160448
CI	0.53	0.026	2735603
L_{bio}	0.44	0.055	12098635
H_{bio}	0.25	0.039	3447152
SN	0.74	0.025	63647

B:			
Surface Type	Mean	Standard Ødeviation	nNumber of observations

WAT	0.0815	0.04839	174791467472
CC	0.1107	0.04134	24072258520
CI	0.467	0.07585	594731440590118
L _{bio}	0.315	0.04229	87401867168162
H _{bio}	0.228	0.02633	2270206
SN	0.76	0.058	16333853

C:

Surface Type	Mean	Standard deviationSD	nNumber of observations
WAT	0.0812	0.04439	52060467885
CC	0.1308	0.03543	345867272419
CI	0.463	0.04248	677176317722683
L _{bio}	0.321	0.04639	249818328388680
H _{bio}	0.230	0.02814	14100954417403
SN	0.609	0.06650	9924812357

D:

Surface Type	Mean	SDstandard deviation	nNumber of observations
CI	0.4550	0.092	22
L _{bio}	0.346	0.07	28
H _{bio}	0.24	0.03	22
SN	0.56	0.10	5

1390 **Table 12:** A) summary of the albedo for each surface class as predicted from our classified UAV image. B) summary of
 1395 the albedo for each surface class as predicted from our classified Sentinel-2 image for 2017. C) summary of the albedo
 for each surface class as predicted from our classified Sentinel-2 image for 2016. D) summary of the broadband
 albedo for each surface class as measured using field spectroscopy at our field site in 2017 (we do not have cosine-
 collector albedo measurements for water or cryoconite surfaces).

	UAV Image	Sentinel 2 (2016)	Sentinel 2 (2017)
Total Image Area (km²)	0.04	19499 <u>10,000</u>	26741 <u>10,000</u>
Total Algae (%)	78.5	0.61 <u>57.99</u>	0.19 <u>58.87</u>
H_{bio} (%)	17.4	0.09 <u>8.35</u>	0.04 <u>2.54</u>
L_{bio} (%)	61.08	0.52 <u>49.65</u>	56.33 <u>0.15</u>
Cryoconite (%)	0.82	0.01 <u>1.61</u>	1.67 <u>0.01</u>
Clean Ice (%)	13.81	0.37 <u>40.08</u>	0.80 <u>38.34</u>
Water (%)	0.78	0.01 <u>0.31</u>	1.13 <u><0.01</u>
<u>Snow (%)</u>	<u>6.09</u>	<u>n/a</u>	<u>n/a</u>

1400 **Table 23:** percentage of each image covered by each surface type as predicted by our trained RF algorithm. Snow was
 removed from the calculation in the Sentinel-2 images to enable quantification of surface coverage in the bare-ice
 zone, i.e. below the snow line, only.

1405



Figure 1: The logo of Copernicus Publications.